The Astrophysical Journal, 959:12 (22pp), 2023 December 10 https://doi.org/10.3847/1538-4357/acfeeb

Probing the Low-mass End of Core-collapse Supernovae Using a Sample of Strongly-stripped Calcium-rich Type IIb Supernovae from the Zwicky Transient Facility

Kaustav K. Das[1], Mansi M. Kasliwal[1], Christoffer Fremling[1], Sheng Yang[2], Steve Schulze[3], Jesper Sollerman[2], Tawny Sit[1], Kishalay De[4], Anastasios Tzanidakis[1], Daniel A. Perley[5], Shreya Anand[6], Igor Andreoni[7,8,9], C. Barbarino[2], K. Brudge[1], Andrew Drake[1], Avishay Gal-Yam[10], Russ R. Laher[11], Viraj Karambelkar[1], S. R. Kulkarni[1], Frank J. Masci[11], Michael S. Medford[12,13], Abigail Polin[1], Harrison Reedy[1], Reed Riddle[1], Yashvi Sharma[1], Roger Smith[14], Lin Yan[14], Yi Yang[1], and Yuhan Yao[1]

[1] Cahill Center for Astrophysics, California Institute of Technology, MC 249-17, 1200 E. California Boulevard, Pasadena, CA 91125, USA; kdas@astro.caltech.edu
[2] The Oskar Klein Centre, Department of Astronomy, Stockholm University, AlbaNova, SE-10691 Stockholm, Sweden
[3] The Oskar Klein Centre, Department of Physics, Stockholm University, AlbaNova, SE-10691 Stockholm, Sweden
[4] MIT-Kavli Institute for Astrophysics and Space Research, 77 Massachusetts Avenue, Cambridge, MA 02139, USA
[5] Astrophysics Research Institute, Liverpool John Moores University, IC2, Liverpool Science Park, Liverpool L3 5RF, UK
[6] Division of Physics, Mathematics and Astronomy, California Institute of Technology, Pasadena, CA 91125, USA
[7] Joint Space-Science Institute, University of Maryland, College Park, MD 20742, USA
[8] Department of Astronomy, University of Maryland, College Park, MD 20742, USA
[9] Astrophysics Science Division, NASA Goddard Space Flight Center, Mail Code 661, Greenbelt, MD 20771, USA
[10] Department of Particle Physics and Astrophysics, Weizmann Institute of Science, 234 Herzl Street, 76100 Rehovot, Israel
[11] IPAC, California Institute of Technology, 1200 E. California Boulevard, Pasadena, CA 91125, USA
[12] Department of Astronomy, University of California, Berkeley, CA 94720, USA
[13] Lawrence Berkeley National Laboratory, 1 Cyclotron Road, Berkeley, CA 94720, USA
[14] Caltech Optical Observatories, California Institute of Technology, Pasadena, CA 91125, USA

Received 2022 October 24; revised 2023 September 16; accepted 2023 September 18; published 2023 November 29

Abstract

The fate of stars in the zero-age main-sequence (ZAMS) range ≈8–12 $M_\odot$ is unclear. They could evolve to form white dwarfs or explode as electron-capture supernovae (SNe) or iron core-collapse SNe (CCSNe). Even though the initial mass function indicates that this mass range should account for over 40% of all CCSN progenitors, few have been observationally confirmed, likely due to the faintness and rapid evolution of some of these transients. In this paper, we present a sample of nine Ca-rich/O-poor Type IIb SNe detected by the Zwicky Transient Facility with progenitors likely in this mass range. These sources have a [Ca II] $\lambda\lambda$7291, 7324/[O I] $\lambda\lambda$6300, 6364 flux ratio of $\gtrsim$2 in their nebular spectra. Comparing the measured [O I] luminosity ($\lesssim 10^{39}$ erg s^{-1}) and derived oxygen mass ($\approx 0.01\ M_\odot$) with theoretical models, we infer that the progenitor ZAMS mass for these explosions is less than 12 $M_\odot$. The ejecta properties ($M_{\rm ej} \lesssim 1\ M_\odot$ and $E_{\rm kin} \sim 10^{50}$ erg) are also consistent. The low ejecta mass of these sources indicates a class of strongly-stripped SNe that is a transition between the regular stripped-envelope SNe and ultra-stripped SNe. The progenitor could be stripped by a main-sequence companion and result in the formation of a neutron star–main sequence binary. Such binaries have been suggested to be progenitors of neutron star–white dwarf systems that could merge within a Hubble time and be detectable with LISA.

Unified Astronomy Thesaurus concepts: Supernovae (1668); Core-collapse supernovae (304); Compact binary stars (283)

Supporting material: machine-readable tables

1. Introduction

The fate of stars with zero-age main-sequence (ZAMS) masses larger than ≈12 $M_\odot$ is reasonably well understood from stellar evolution theory and observations. They form a massive iron core and may explode as a core-collapse supernova (CCSN) once their cores reach the Chandrasekhar mass. However, the fate of less massive stars in the ZAMS range ≈8–12 $M_\odot$ is less clear (e.g., Janka 2012). They might form white dwarfs (WD), explode as electron-capture SNe with an ONeMg core (e.g., Nomoto 1984; Stockinger et al. 2020), or form an iron core like regular massive stars. Depending on the metallicity and mass loss in binary systems, these stars might undergo violent flashes and power unusual transients before their deaths (Woosley & Heger 2015; Pumo et al. 2009; Podsiadlowski et al. 2004).

We expect that the narrow range of ZAMS masses from ≈8 to 12 $M_\odot$ should account for a significant fraction of CCSNe, given that the initial mass function (IMF) of stars drops rapidly toward high masses. For a typical IMF, we expect over 40% of the potential CCSN progenitors to reside in this mass range (Sukhbold et al. 2016). However, surprisingly, the number of SNe associated with a low-mass progenitor is small, with most of them being low-luminosity Type II SNe (e.g., Yang et al. 2021; O'Neill et al. 2021; Reguitti et al. 2021; Valerin et al. 2022; Kozyreva et al. 2022). Despite higher abundance in the universe, transients with low-mass progenitors may be missed because they are faint and evolve rapidly. The low-mass end of the CCSN population is expected to be underenergetic and possibly underluminous (Melson et al. 2015; Nomoto et al. 1982). Thus, there is likely an observational bias due to the challenge of discovering and follow-up of such faint and rapidly evolving transients. It is difficult to understand the explosion mechanisms and trends for this population owing to the small number of detections.

In this paper, we present a sample of Ca-rich Type IIb SNe, with potential progenitor mass lying in this low mass range, detected by the Zwicky Transient Facility (ZTF; Bellm et al. 2019; Graham et al. 2019). Type IIb is a class of CCSNe whose progenitors initially exhibit hydrogen spectral features that weaken and disappear in the weeks following explosion. Unlike Type II SNe, which are associated with red supergiant progenitors with ZAMS mass ranging from 8 to 20 $M_{\odot}$ (see Smartt et al. 2009, 2015; Van Dyk 2017, for a review), the mechanisms that drive the stripping and the regimes in which they dominate are still open questions for Type IIb SNe (e.g., Sravan et al. 2019).

Ca-rich transients are a class of SNe that are identified by a high [Ca II]/[O I] flux ratio (>2) in the nebular phase. Because the oxygen that we see in the nebular phase is formed primarily in the hydrostatic burning phase of the progenitor, its mass depends sensitively on the progenitor mass and is smaller for lower-mass progenitors. Calcium, on the other hand, is synthesized by oxygen burning at a later stage and has a relatively weak dependence on progenitor mass. Thus, the Ca/O ratio acts as a tracer for the progenitor mass of CCSNe (Fransson & Chevalier 1989; Jerkstrand et al. 2014, 2015; Prentice et al. 2022; Fang et al. 2022; Ergon & Fransson 2022), and a high Ca/O flux ratio implies a lower abundance of oxygen. The typical Type I Ca-rich transients are generally discovered in the outskirts of early-type galaxies (Perets et al. 2011; Kasliwal et al. 2012; Lunnan et al. 2017). Their old environments make CCSNe unlikely to be the cause for these transients (Perets et al. 2011). However, the SNe in our sample are different from the usual Type I Ca-rich gap transients; they are found in star-forming regions and are classified as Type IIb SNe based on the photospheric spectra.

Recently, SN 2019ehk was proposed to be a Ca-rich Type IIb SN from a low-mass stripped progenitor (De et al. 2021). This is unusual since CCSNe usually have a low [Ca II]/[O I] ratio. SN 2019ehk was discovered in the galaxy M100 (Grzegorzek 2018; Jacobson-Galán et al. 2020, 2021). Jacobson-Galán et al. (2020) suggested a thermonuclear explosion origin arising from a low-mass hybrid HeCO WD + CO WD merger. However, a core-collapse explosion from a <10 $M_{\odot}$ ZAMS star could not be ruled out from archival Hubble Space Telescope images. Nakaoka et al. (2021) suggested that SN 2019ehk originated in an ultra-stripped CCSN (USSN). However, we do not expect to see hydrogen in an USSN. Thus, Ca-rich IIb events could potentially be strongly stripped SNe (SSSNe), which is a transition class between the regular stripped-envelope SNe (SESNe) and USSNe.

Here we present a holistic analysis of the light-curve and spectral properties for a sample of nine strongly stripped Ca-rich Type IIb SNe. This work is useful to describe these potentially common types of transients, understand the fate of the low-mass end of CCSNe, and determine the evolutionary pathway for Type IIb SNe. In addition, this sample increases the number of Ca-rich Type IIb SNe observed in the literature from 1 to 9. They could provide observational constraints on SN explosions of low-mass He stars. It can also help probe the distribution of the degree of stripping, understand common envelope evolution, and constrain rates of binary mergers such as neutron star (NS)−WD systems that could be detectable in gravitational waves.

The sample selection and data used are described in Section 2. In Section 3, we present our analysis of the late-time nebular spectra, photospheric spectra, light curves, and the host galaxy photometry of the sample. We discuss the inferred progenitor properties, evolutionary pathways, and rates in Section 4. We provide a brief summary of the results and future goals in Section 5.

2. Data

2.1. Sample Selection

In this work, we use SNe detected by ZTF. ZTF has a 47 deg^2 field-of-view camera (Dekany et al. 2020) that is mounted on the Palomar 48-inch (P48) Oschin Schmidt telescope. It images the entire northern sky every ∼2 nights in *g* and *r* bands, with a median depth of around 20.5 mag. We use ZTF discoveries that are part of the Bright Transient Survey (BTS; Fremling et al. 2020), a magnitude-limited survey aimed at spectroscopically classifying all SNe with peak magnitude brighter than 18.5 mag, and the Census of the Local Universe (CLU) survey (De et al. 2020), a volume-limited survey aimed at classifying all SNe within 200 Mpc whose hosts belong to the CLU galaxy catalog (Cook et al. 2019).

We apply the following selection criteria to the ZTF SN sample obtained from the BTS and the CLU survey (until 2021 December 31):

1. The transient should be classified as a Type IIb SN based on spectra obtained near peak light. We have 94 Type IIb SNe in the BTS + CLU sample.
2. We obtained at least one epoch of late-time nebular spectroscopy (at >50 rest-frame days post-explosion) for events satisfying the above criteria. This was true for 29 of the 94 Type IIb SNe.
3. The [Ca II]/[O I] ratio in the nebular-phase spectrum should be >2 (Milisavljevic et al. 2017; De et al. 2018). This is true for 11 out of the 29 SNe for which we have nebular spectra. We excluded two SNe[15] because of poor light-curve quality. Table 1 lists the general properties of the nine SNe in the final sample.

2.2. Optical Photometry

We perform forced point-spread function photometry on the ZTF difference images via the ZTF forced-photometry service (Masci et al. 2019) in *g*, *r*, and *i* bands. For this work, we consider anything less than a 3σ detection an upper limit. The ZTF light curves were supplemented with photometry from the Palomar 60-inch telescope (P60; Cenko et al. 2006), the Optical wide field camera on the Liverpool Telescope (LT; Steele et al. 2004), and Sinistro and SBIG imagers on the 1 m class telescopes and the Spectral imager on the 2 m class telescopes operated by Las Cumbres Observatory (LCO; Brown et al. 2013) in *g*, *r*, and *i* bands. We also use photometry in *u*, *i*, and *z* bands obtained with the LT for a few sources. These data were processed with the automatic image subtraction pipeline FPipe (Fremling et al. 2016) using reference images from the Sloan Digital Sky Survey (SDSS; Ahn et al. 2012) and Pan-STARRS (PS1; Chambers et al. 2016). We have early-time UV data from the Ultra-Violet/Optical Telescope (UVOT; Roming et al. 2005), which is on board the Neil Gehrels Swift Observatory (Gehrels et al. 2004). The UVOT

---

[15] SN 2019lsk, SN 2019rta.

Table 1
Summary of the Sample of SNe Presented in This Work

ZTF Name	IAU Name	R.A. (hh:mm:ss)	Decl. (dd:mm:ss)	Redshift	$t_{\max 1}$ (MJD)	M_{r1} (mag)	$t_{\max 2}$ (MJD)	M_{r2} (mag)	Av,MW	Av,host
ZTF19aatesgp	SN 2019ehk	12:22:56.14	+15:49:34.0	0.006	58606	−18.2	58616	−17.9	0.1	2.2
ZTF21aaabwfu	SN 2021M	14:14:14.72	+35:25:23.1	0.011	59216	−16.8	59231	−17.0	0.1	2.1
ZTF20abwzqzo	SN 2020sbw	02:46:03.31	+03:19:47.6	0.023	59088	−16.9	59104	−17.9	0.1	0.7
ZTF21aabxjqr	SN 2021pb	09:44:46.80	+51:41:14.6	0.033	59221	−16.9	59238	−16.8	0.0	0.0
ZTF19abxtcio	SN 2019pof	01:12:37.87	+33:02:05.7	0.015	58733	−15.6	58749	−16.7	0.2	0.5
ZTF18abwkrbl	SN 2018gjx	02:16:15.58	+28:35:28.6	0.012	58379	−17.8	58390	−16.9	0.2	0.0
ZTF19abacxod	SN 2019hvg	14:06:01.58	+12:46:50.3	0.018	58654	−16.6	58672	−17.6	0.1	0.8
ZTF18acqxyiq	SN 2018jak	09:59:18.19	+34:53:43.7	0.038	58447	−18.1	58467	−17.5	0.0	0.6
ZTF21abjyiiw	SN 2021sjt	20:37:19.19	+66:06:23.1	0.005	59403	−16.9	59417	−16.7	1.0	1.9

Note. Subscripts 1 and 2 refer to the peak parameters of the first peak and second peak, respectively. The absolute magnitudes are corrected for Milky Way and host galaxy extinction (see Section 3.1).

data are reduced using HEASOFT.[16] We also use forced-photometry data points from the Asteroid Terrestrial-impact Last Alert System (ATLAS; Tonry et al. 2018; Smith et al. 2020). Figure 1 shows a multipaneled figure of the light curves for the SNe in our sample.

2.3. Optical Spectroscopy

We obtained spectroscopy at multiple epochs for the sources in our sample, with phases varying from 1 day to over 200 days past the explosion day. One spectrum is obtained near peak luminosity for initial spectroscopic classification. Further spectral follow-up is part of the classification effort of the BTS and the CLU survey. We primarily use the Double Beam Spectrograph (DBSP; Oke & Gunn 1982) on the Palomar 200-inch telescope and the Spectral Energy Distribution Machine (SEDM; Blagorodnova et al. 2018; Rigault et al. 2019) on the Palomar 60-inch telescope for classification. The DBSP spectra reduction pipelines used are described in Bellm & Sesar (2016) and Roberson et al. (2022). The SEDM data reduction pipeline is described in Rigault et al. (2019). We also use spectra from the Spectrograph for the Rapid Acquisition of Transients (SPRAT; Piascik et al. 2014) on the Liverpool Telescope, the Alhambra Faint Object Spectrograph and Camera (ALFOSC) on the Nordic Optical Telescope (NOT; Djupvik & Andersen 2010), and the Device Optimized for the LOw RESolution (DOLORES) on the Telescopio Nazionale Galileo (TNG). The SPRAT pipeline is based on the FrodoSpec pipeline (Barnsley et al. 2012). The NOT and TNG data were reduced using the data reduction pipelines PyNOT[17] and PypeIt (Prochaska et al. 2020). Late-time nebular-phase spectra were obtained using the Low Resolution Imaging Spectrometer (LRIS) on the Keck I telescope starting ≈50 days post-explosion. For a couple of sources, we obtained multiple epochs of nebular-phase spectra using LRIS. The LRIS spectra were reduced using the automated LPIPE (Perley 2019) pipeline. We used a publicly available LRIS spectrum for SN 2021sjt from 2021 July 8 (Siebert et al. 2021). Table 3 lists the log of the observed spectra. Figure 2 shows one photospheric spectrum obtained for each source, and Figure 3 shows the obtained nebular spectra.

2.4. Host Photometry

We obtain science-ready coadded images from the Galaxy Evolution Explorer (GALEX) general release 6/7 (Martin et al. 2005), SDSS data release 9 (SDSS DR9; Ahn et al. 2012), the Two Micron All Sky Survey (2MASS; Skrutskie et al. 2006), the Panoramic Survey Telescope and Rapid Response System (Pan-STARRS, PS1) Data Release 1 (Chambers et al. 2016), and preprocessed WISE images (Wright et al. 2010) from the unWISE archive (Lang 2014).[18] The unWISE images are based on the public WISE data and from the ongoing NEOWISE-Reactivation mission R3 (Mainzer et al. 2014; Meisner et al. 2017). We measure the brightness of the host galaxies using the Lambda Adaptive Multi-Band Deblending Algorithm in R (LAMBDAR;[19] Wright et al. 2016) and the methods described in Schulze et al. (2021). We use the offsets reported by Blanton & Roweis (2007) and Cutri et al. (2013) to convert the 2MASS and unWISE photometry from the Vega system to the AB system.

3. Methods and Analysis

3.1. Extinction Correction

We need an estimate of the extinction of the SN light due to dust along the line of sight to the observer in order to accurately estimate its explosion parameters. Extinction is typically split into two components. The first Galactic component accounts for extinction due to dust within the Milky Way, and the second component accounts for extinction external to the Milky Way, mostly attributed to the host galaxy of the SNe. We correct for Galactic extinction by using the reddening maps of Schlafly & Finkbeiner (2011). We use the Cardelli et al. (1989) extinction law and $R_V = 3.1$ for reddening corrections. Accounting for extinction external to our own Galaxy is more challenging. In this paper, we use two different approaches to correct for the host extinction.

---

[16] https://heasarc.gsfc.nasa.gov/docs/software/heasoft

[17] https://github.com/jkrogager/PyNOT

[18] http://unwise.me

[19] https://github.com/AngusWright/LAMBDAR

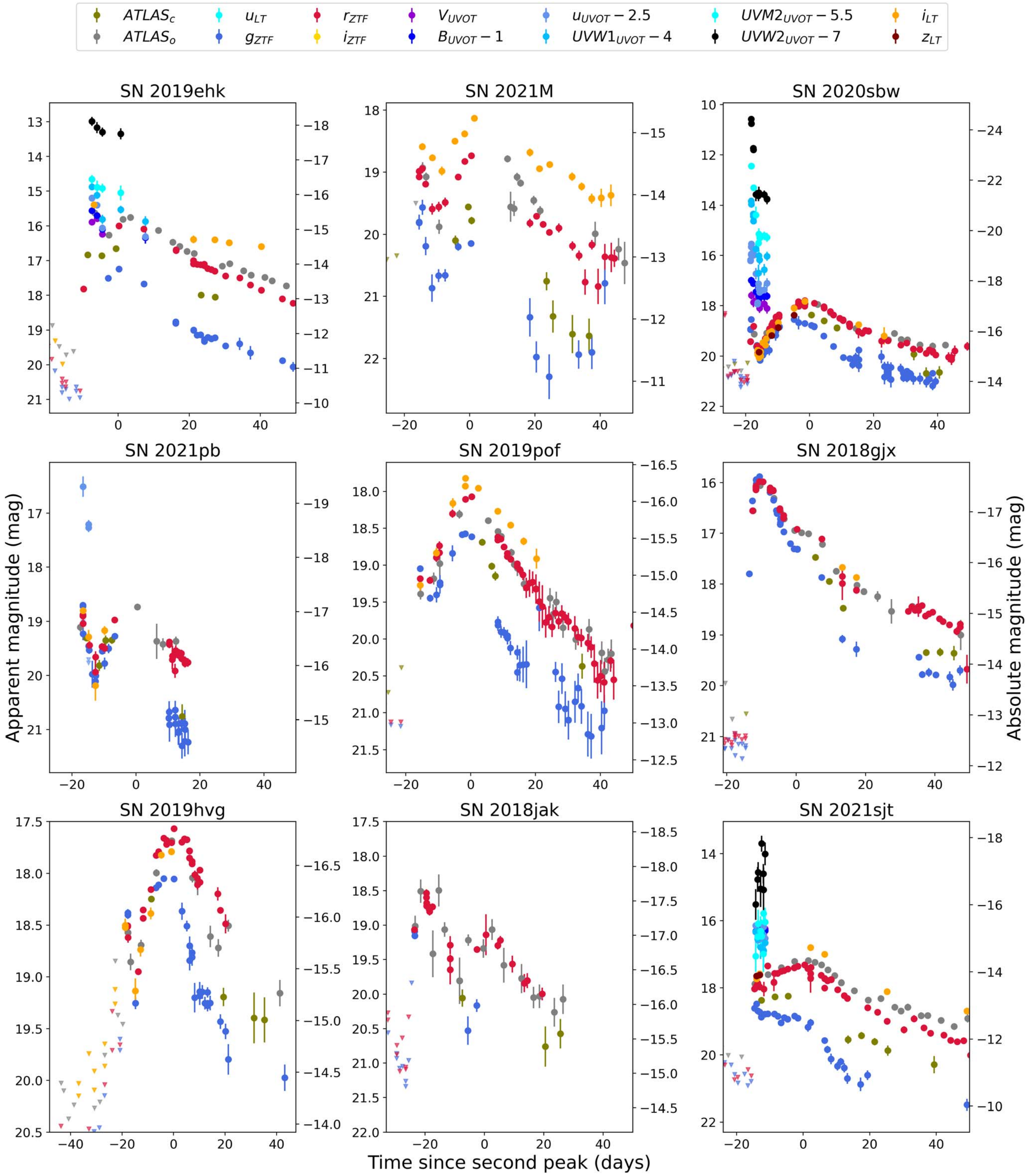

Figure 1. Light curves for our sample of nine Ca-rich Type IIb SNe. This has forced-photometry from ZTF, ATLAS, and follow-up observations from various instruments. See Section 2.2 for further description on the photometry. The left *y*-axis shows the apparent magnitude (mag), and the right *y*-axis shows the absolute magnitude (mag), without host extinction correction. The *x*-axis shows the number of rest-frame days since the second peak.

First, we use the intrinsic color template from the Carnegie Supernova Project (CSP-I; Stritzinger et al. 2018). This assumes that Type IIb SNe show similar intrinsic colors after peak. We measure the average difference of our observed colors and the intrinsic template between 0 and 20 days after *r*-band peak as the excess color due to host extinction. We use $R_V = 3.1$ and the Cardelli et al. (1989) extinction law to correct for the reddening. Shock-cooling breakout modeling (described in Section 3.4.2) provides an opportunity to put an upper limit to the host extinction value. When we use host extinction using the CSP template for SN 2021sjt, we get an unphysically large progenitor envelope radius ($R_{\rm env}$) of around $1.7 \times 10^6\,R_\odot$. Thus, we need to be cautious while using the intrinsic template given by Stritzinger et al. (2018) based on a sample size of three Type IIb SNe.

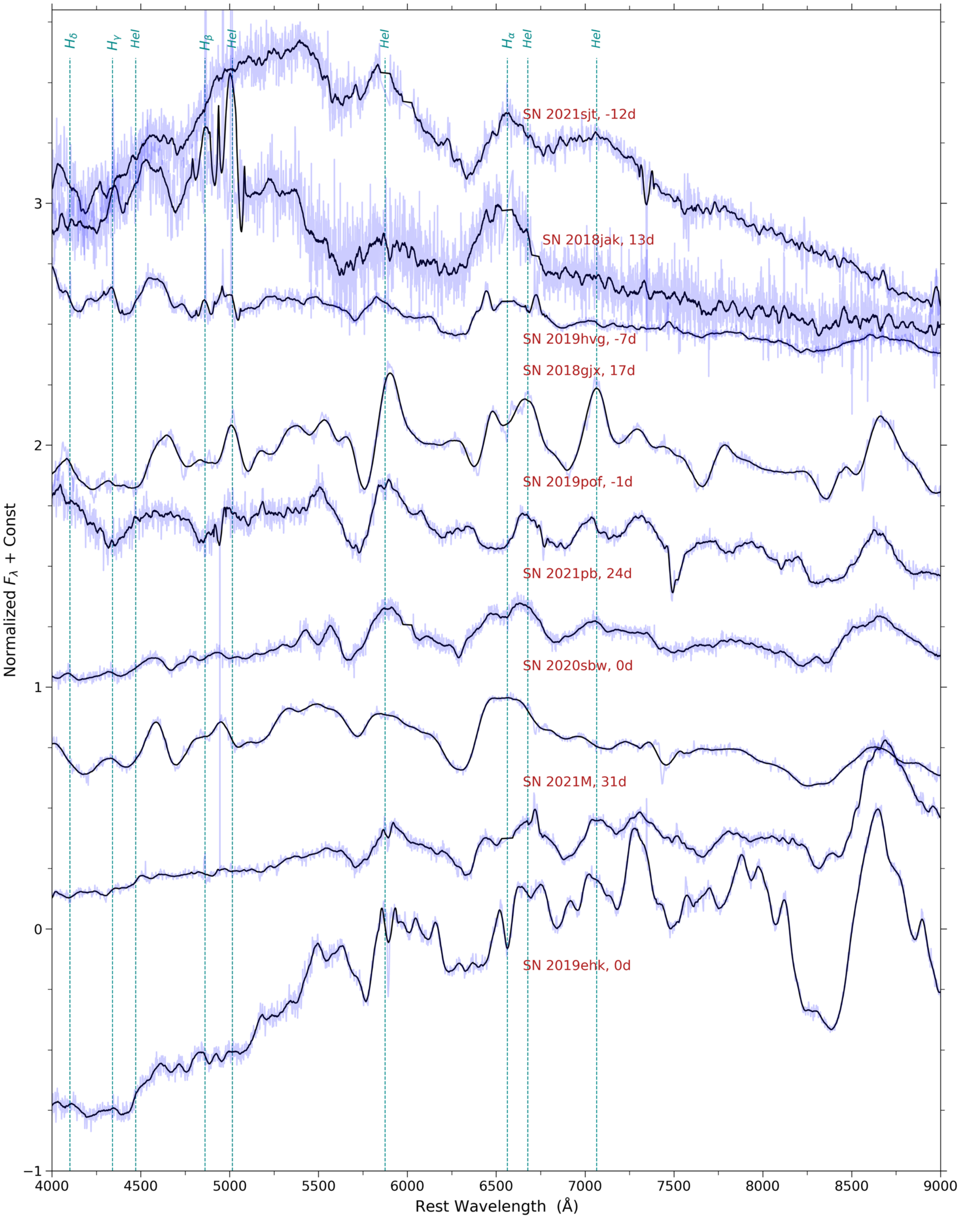

Figure 2. Collage of a few spectra for the SNe in our sample showing H and He emission lines. The phase of the spectra is measured as the number of rest-frame days since the second peak.

Second, we use the narrow host galaxy absorption lines of Na I D. This assumes that there is a relation between host galaxy sodium absorption lines and the amount of extinction (Poznanski et al. 2012; Stritzinger et al. 2018). To compute the Na I D equivalent width (EW), we use spectra obtained with DBSP, ALFOSC, and LRIS, where the signal-to-noise ratio of the spectrum allows the measurement of the EW. To compute A_V, we use $A_V^{\mathrm{host}}[\mathrm{mag}] = 0.78(\pm 0.15) \times \mathrm{EW}_{\mathrm{Na\ I\ D}}[\mathrm{Å}]$ reported in Stritzinger et al. (2018). We note that the Na I D EW measurement is not always a reliable tracer of the host extinction. This is particularly true for low-resolution spectra (Poznanski et al. 2011) and in the presence of circumstellar material (Phillips et al. 2013).

The extinction values measured as described are shown in Table 2. For the light-curve analysis done in this paper, we use the average of the extinction values we get from these methods.

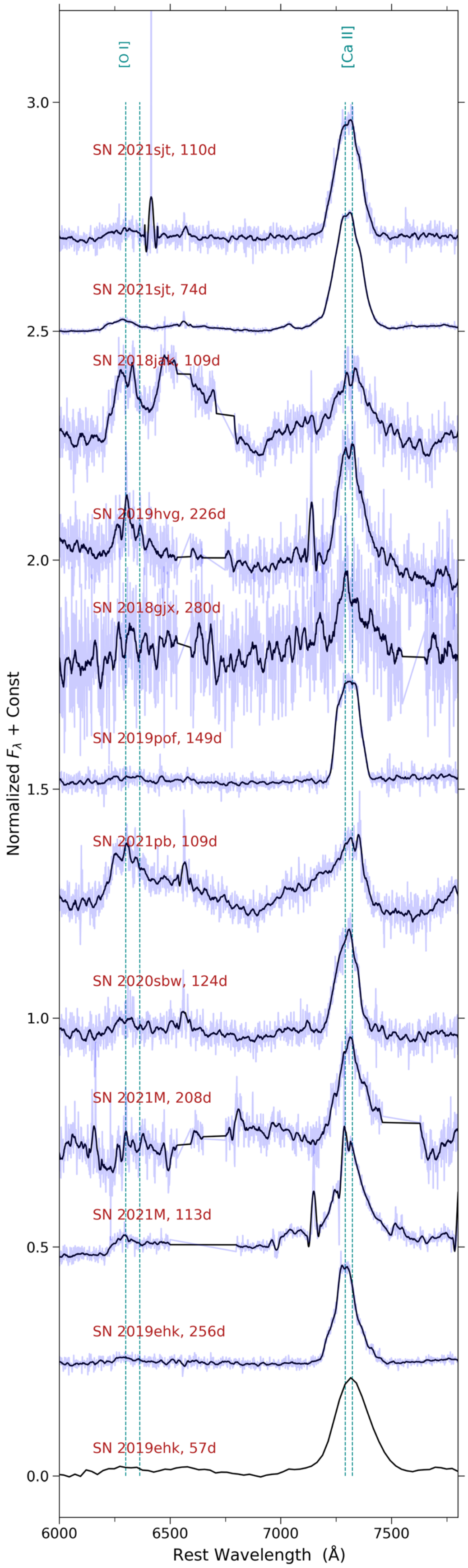

Figure 3. Nebular spectra showing the [Ca II] $\lambda\lambda$7291, 7324 and [O I] $\lambda\lambda$6300, 6364 lines. The phase of the spectra is measured as the number of rest-frame days since the second peak. The spectra with the full wavelength range are shown in Appendix A.

We show the color evolution of our objects compared to the Type IIb SN sample of Taddia et al. (2018) in Appendix A.

3.2. Photospheric Spectra

As described in Section 2.3, we obtain spectra close to the peak epoch for all the sources. Classifications were done using the `SuperNova Identification` (`SNID`; Blondin & Tonry 2007) code. We used the `superfit` (Howell et al. 2005) code to classify spectra contaminated by the host galaxy. The final classification as Type IIb was made after manual inspection of the emission and absorption lines and the best-fit templates matched from `SNID` or `superfit`.

We determine the expansion velocities of the H I λ6563, He I λ5876, and O I λ7774 lines where absorption from these lines could be identified and measurements were possible. To do this, we fit the minima of the absorption part of the P Cygni profiles of the spectral lines with a polynomial fit (with the polynomial degree manually tuned for each spectrum, but typically 3). The minima of the absorption features are then used to estimate the expansion velocity. For certain cases, where the spectra are contaminated with galaxy lines or the resolution is not high, we find the minima of the absorption portion by manual inspection. We list the velocities obtained in Table 3. To estimate uncertainties on our measurements, we use a Monte Carlo approach. We obtain a noise spectrum by subtracting a heavily smoothed version of the spectrum from the original spectrum. To get an estimate of the noise, we then calculate the standard deviation of this noise spectrum. Then, we create simulated noisy spectra by adding noise using a standard Gaussian distribution with the standard deviation calculated above. To the heavily smoothed spectra, we add these simulated noise spectra and recalculate the velocity from the absorption minima for each simulated spectrum. The standard deviation of these measurements is taken as the 1σ uncertainty of our velocity measurements. Fremling et al. (2018) analyzed the spectra of a sample of 55 Type IIb SNe discovered by the Palomar Transient Factory (PTF) and intermediate PTF (iPTF) surveys. We compare the velocities we have with the mean velocities obtained in Fremling et al. (2018) for the He I λ5876 line. From Figure 4, we find that the expansion velocities obtained using the He I λ5876 line are consistent with those of typical Type IIb SNe obtained by Fremling et al. (2018).

3.3. Nebular Spectra

We obtained late-time photometry using the LCO, Keck, P60, and P48 telescopes as recorded in Table 4. Since the [Ca II] line lies entirely in the i band, the interpolated late-time photometry is used to flux-calibrate our nebular spectra. When late-time photometry is not available, we extrapolate the light curve by assuming a late-time (>30 days) i-band decline rate of 0.019 ± 0.004 mag day^{-1}, based on the average late-time decay of the SESNe tabulated in Wheeler et al. (2015).

We measure the line fluxes by numerical integration of the respective wavelength regions. We add noise (scaled to nearby regions of the continuum) to the line profile and use Monte Carlo sampling of the estimated fluxes to quantify the uncertainties. The measured [Ca II] $\lambda\lambda$7291, 7324 and [O I] $\lambda\lambda$6300, 6364 fluxes and their ratio are shown in Table 4.

Table 2
Summary of the Host Extinction Parameters for Our Sample

Source	Telescope + Instrument	Date	Na I D EW (Å)	Avg. Color ($g - r$) (mag)	$A_{V,\ \mathrm{Na\ I\ D}}$ (mag)	$A_{V,\ \mathrm{color}}$ (mag)	A_V Used (mag)
SN 2019ehk	P200+DBSP	13 May 2019	2.99 ± 0.27	0.68 ± 0.03	2.3(0.2)	2.3(0.2)	2.2
	Keck I+LRIS	3 Jun 2019	2.55 ± 0.43		2.0(0.3)		
SN 2021M	Keck I+LRIS	12 Jan 2021	2.03 ± 0.22	0.95 ± 0.4	1.6(0.2)	3.2(0.3)	2.1
	Keck I+LRIS	17 Feb 2021	2.37 ± 0.21		1.8(0.2)		
	Keck I+LRIS	10 May 2021	2.12 ± 0.24		1.7(0.2)		
	Keck I+LRIS	13 Aug 2021	2.71 ± 0.41		2.1(0.3)		
SN 2020sbw	NOT+ALFOSC	14 Sep 2020	<0.1	0.51 ± 0.10	<0.1	1.4(0.1)	0.7
SN 2021pb	···				···	···	0
SN 2019pof	···			0.38 ± 0.11	···	0.5(0.1)	0.5
SN 2018gjx	···				···	···	0
SN 2019hvg	···			0.59 ± 0.21	···	0.8(0.1)	0.8
SN 2018jak	Keck I+LRIS	4 Dec 2018	0.8 ± 0.35		0.6(0.3)	···	0.6
SN 2021sjt	Keck I+LRIS	8 Jul 2021	2.31 ± 0.15	1.1 ± 0.2	1.8(0.1)	3.3(0.3)	1.9
	P200+DBSP	10 Jul 2021	2.39 ± 0.19		1.9(0.1)		
	P200+DBSP	07 Aug 2021	1.57 ± 0.24		1.2(0.2)		
	Keck I+LRIS	12 Aug 2021	1.50 ± 0.31		1.2(0.2)		

3.4. Modeling Light Curves

3.4.1. Blackbody Fit

We estimate the bolometric light curve at epochs where at least detections in two filters are available by fitting a blackbody function. For each epoch, we do the blackbody fit using a Markov Chain Monte Carlo method using the Python EMCEE package (Foreman-Mackey et al. 2013) to estimate the temperature, radius, and bolometric luminosity. We use the 16th and 84th percentiles of the posterior probability distribution as the model uncertainties. The blackbody fits for each source are available in Appendix D.

3.4.2. Modeling the Shock-cooling-powered Emission Peak

All the sources in our sample have a double-peaked light curve, which is usually seen in Type IIb SNe. The timescale of the first peak, the initial blue color, and high temperatures indicate that the first peak is dominated by cooling emissions from the shock-heated extended envelope (Rabinak & Waxman 2011; Nakar & Piro 2014; Piro 2015). We note that some of the SNe from our sample do not have well-sampled first peaks on both the rising and fading parts. We use the model by Piro et al. (2021) to fit for the shock-cooling breakout peak. This model constrains the extended material radius (R_{ext}), mass (M_{ext}), and energy (E_{ext}) and the explosion time (t_{exp}). We first select the appropriate epochs of the light-curve peaks to model as shock cooling, and then we fit the multiband data using the Python EMCEE package. The best-fit values and fits for each source are provided in Table 5 and Appendix B.

3.4.3. Modeling the Radioactively Powered Light-curve Peak

After fitting the initial cooling peaks in our light curves, we use the best-fit parameters to estimate the contribution of the cooling emission to the bolometric light curve of each source. We then subtract the cooling component from the bolometric light curves obtained from blackbody fitting. The subtracted light curves now correspond to that of the radioactively powered peak. We fit for this peak using two methods. First, we use the analytical model described in Arnett et al. (1989) and Valenti et al. (2008). We attempt to constrain the nickel mass (M_{Ni}), characteristic photon diffusion timescale (τ_m), and characteristic γ-ray diffusion timescale (t_o). We use relations from Wheeler et al. (2015) that give the ejecta mass (M_{ej}) and kinetic energy in the ejecta (E_{kin}) as a function of (τ_m) and photospheric velocity (v_{ph}). We obtain v_{ph} measured using the He I line from the photospheric spectra closest to the peak epoch as described in Section 3.2. We also use the light-curve analytical models from Khatami & Kasen (2019) to derive the explosion parameters. Further details on the model fitting can be found in Appendix B9 in Yao et al. (2020). Table 6 lists the best-fit parameters. Figures 5 and 6 show the comparison of the cumulative distribution functions for M_{Ni} and M_{ej} of our sample and the Taddia et al. (2018) sample of Type IIb SNe. A two-sided K-S test of the ejecta mass distribution gives a p-value <0.001, thus implying that our sample contains SNe with lower ejecta mass compared to the literature sample of SNe IIb. Our sample indicates that there is an empty phase space with low ejecta mass but high nickel mass and high ejecta mass but low nickel mass (see Figure 7). Further analysis on this with a larger sample of Type IIb SNe is left for future work. We plot the light curves of the Ca-rich Type IIb SN sample along with canonical Type IIb SNe from Taddia et al. (2018) in Figure 8.

3.5. Host Galaxy Spectral Energy Distribution Modeling

We model the spectral energy distributions (SEDs) of the host galaxies with the software package Code Investigating GALaxy Evolution (CIGALE; Burgarella et al. 2005; Noll et al. 2009; Boquien et al. 2019). We use the Chabrier (2003) IMF and the Bruzual & Charlot (2003) simple stellar population model to compute the stellar emission. Furthermore, we assume a star formation history (SFH) with the following functional form: $t \times \exp(-t/\tau)$, where t is the age of the SFH episode

Table 3

Log of the Spectral Observations and Expansion Velocity for a Few Spectral Lines in km s^{-1}

Object	Instrument	Range (Å)	Date	Phase (days)	H I λ6563 (km s^{-1})	He I λ5876 (km s^{-1})	O I λ7774 (km s^{-1})
SN 2021M	P60+SEDM	3500–9220	10 Jan 2021	···7	18100 ± 4200	···	···
	Keck I+LRIS	3200–10 000	12 Jan 2021	−5	14500 ± 300	11000 ± 1900	···
	Keck I+LRIS	3200–10 000	17 Feb 2021	+31	12400 ± 100	8400 ± 200	3700 ± 300
	Keck I+LRIS	3200–10 000	10 May 2021	+113	···	9100 ± 2700	4700 ± 1600
	Keck I+LRIS	3200–10 000	13 Aug 2021	+208	···	···	2900 ± 900
SN 2020sbw	P200+DBSP	3200–10 100	29 Aug 2020	−14	···	···	···
	P60+SEDM	3500–9220	12 Sep 2020	0	13400 ± 1000		
	NOT+ALFOSC	3974–9153	14 Sep 2020	+2	13200 ± 100	7900 ± 100	···
	P60+SEDM	3500–9220	30 Sep 2020	+18	11400 ± 4100	9300 ± 3200	···
	P60+SEDM	3500–9220	7 Oct 2020	+25	···	···	···
	NOT+ALFOSC	3974–9153	16 Oct 2020	+34	13100 ± 200	8900 ± 200	···
	Keck I+LRIS	3200–10 000	14 Jan 2021	+124	···	···	···
SN 2019pof	P60+SEDM	3500–9220	18 Sep 2019	−5	···	···	···
	P200+DBSP	3200–10 100	22 Sep 2019	−1	15200 ± 600	10400 ± 200	···
	Keck I+LRIS	3200–10 000	19 Feb 2020	+149	···	···	···
SN 2019hvg	P60+SEDM	3500–9220	20 Jun 2019	−18	18000 ± 4500	···	···
	P60+SEDM	3500–9220	24 Jun 2019	−14	16200 ± 3900	···	···
	P200+DBSP	3200–10 100	1 Jul 2019	−7	13200 ± 400	9500 ± 400	···
	P60+SEDM	3500–9220	5 Jul 2019	−3	12400 ± 900	10100 ± 2100	···
	Keck I+LRIS	3200–10 000	19 Feb 2020	+226	···	···	···
SN 2019ehk	P60+SEDM	3500–9220	8 May 2019	−5	16500 ± 3200	9900 ± 2300	···
	P200+DBSP	3200–10 100	13 May 2019	0	···	7039 ± 400	···
	Keck I+LRIS	3200–10 000	3 Jun 2019	+21	···	6100 ± 100	···
	P60+SEDM	3200–10 000	9 Jul 2019	+57	···	6200 ± 5100	···
	Keck I+LRIS	3200–10 000	24 Jan 2020	+256	···	···	···
SN 2021pb	P60+SEDM	3200–10 000	7 Jan 2021	−17	···	···	···
	Keck I+LRIS	3200–10 000	11 Jan 2021	−13	18400 ± 2900	17900 ± 2900	···
	Keck I+LRIS	3200–10 000	17 Feb 2021	+24	14300 ± 1800	11100 ± 200	9100 ± 800
	Keck I+LRIS	3200–10 000	13 May 2021	+109	···	7900 ± 2900	6100 ± 2000
SN 2018gjx	P60+SEDM	3200–10 000	18 Sep 2018	−11	···	···	···
	NTT+EFOSC2	3200–10 000	18 Sep 2018	−11	···	···	···
	P60+SEDM	3200–10 000	12 Oct 2018	+13	11100 ± 200	8400 ± 200	4000 ± 600
	NOT+ALFOSC	3974–9153	16 Oct 2018	+17	8300 ± 100	8000 ± 100	3800 ± 100
	Keck I+LRIS	3200–10 000	10 Nov 2018	+42	9400 ± 100	7800 ± 100	4300 ± 100
	TNG+DOLORES	3200–10 000	30 Nov 2018	+62	10500 ± 600	8900 ± 100	7000 ± 400
	Keck I+LRIS	3200–10 000	5 Jan 2019	+98	15100 ± 3400	9300 ± 400	5500 ± 300
	Keck I+LRIS	3200–10 000	6 Jul 2019	+280	···	···	···
SN 2018jak	Keck I+LRIS	3200–10 000	4 Dec 2018	−11	15800 ± 1700	13700 ± 4600	···
	P60+SEDM	3200–10 000	28 Dec 2018	+13	11000 ± 8400	···	···
	Keck I+LRIS	3200–10 000	3 Apr 2019	+109	7500 ± 1200	6600 ± 1500	···
SN 2021sjt	Keck I+LRIS	3200–10 000	8 Jul 2021	−14	10600 ± 1000	···	···
	P60 + SEDM	3200–10 000	8 Jul 2021	−14	···	···	···
	NOT + ALFOSC	3974–9153	8 Jul 2021	−14	11600 ± 3300	···	···
	P200+DBSP	3200–10 100	10 Jul 2021	−12	9900 ± 7600	···	6500 ± 3100
	P60 + SEDM	3200–10 000	10 Jul 2021	−12	···	···	···
	P60 + SEDM	3200–10 000	13 Jul 2021	−9	···	11400 ± 3800	6800 ± 3200
	LT + SPRAT	3200–10 000	17 Jul 2021	−5	5900 ± 1100	10400 ± 1100	6300 ± 100
	P60 + SEDM	3200–10 000	24 Jul 2021	+2	···	11900 ± 7300	···
	NOT + ALFOSC	3974–9153	28 Jul 2021	+6	···	10100 ± 100	5900 ± 200
	P60 + SEDM	3200–10 000	28 Jul 2021	+6	···	12500 ± 3800	7400 ± 2300
	P200+DBSP	3200–10 100	7 Aug 2021	+16	6900 ± 700	···	4300± 900
	Keck I+LRIS	3200–10 000	12 Aug 2021	+21	7400 ± 800	7400 ± 200	···
	P60 + SEDM	3200–10 000	18 Aug 2021	+27	···	···	···
	P60 + SEDM	3200–10 000	23 Sep 2021	+63	···	···	···
	Keck I+LRIS	3200–10 000	4 Oct 2021	+74	···	···	···
	Keck I+LRIS	3200–10 000	9 Nov 2021	+110	···	···	···

Note. The phases are measured as the number of rest-frame days since the second peak.

Table 4
Summary of the Nebular Properties

Source	Spectra Tel.+Inst./Phase (days)	Phot. Tel.+Inst./Phase (days)	Phot. Mag. (mag)	[Ca II]/[O I] Flux Ratio	[O I] Lum. (10^{38}erg s^{-1})	O Mass (10^{-2} $M_\odot$)
SN 2019ehk	Keck I+LRIS/256	Keck I+LRIS/280	22.10 ± 0.15	28.58 ± 3.19	1.72 ± 0.17	3.86–12.91
SN 2021M	Keck I+LRIS/113	LCOGT 1 m/176	21.75 ± 2.19	3.26 ± 1.84	0.15 ± 0.01	0.35–1.12
SN 2021M	Keck I+LRIS/208	LCOGT 1 m/176	21.75 ± 2.19	4.32 ± 0.22	0.93 ± 0.03	2.25–6.58
SN 2020sbw	Keck I+LRIS/124	LCOGT 1 m/115	>20.63	10.37 ± 4.65	<11.69	<17.29
SN 2021pb	Keck I+LRIS/109	LCOGT 1 m/27	>20.21	1.73 ± 0.04	<6.32	<15.58
SN 2019pof	Keck I+LRIS/149	P48/20	19.02 ± 0.30	32.37 ± 1.47	0.01 ± 0.00	0.04–0.10
SN 2018gjx	Keck I+LRIS/102	P60/98	19.61 ± 0.21	2.24 ± 0.51	0.08 ± 0.02	0.16–0.64
SN 2019hvg	Keck I+LRIS/226	P48/43	19.35 ± 0.19	3.69 ± 0.48	0.11 ± 0.01	0.25–0.79
SN 2018jak	Keck I+LRIS/109	P48/109	>20.17	1.60 ± 0.13	<8.57	<20.78
SN 2021sjt	Keck I+LRIS/110	LCOGT 1 m/110	19.39 ± 0.20	10.13 ± 0.86	1.15 ± 0.08	2.68–8.42

Note. The phases are measured as the number of rest-frame days since the second peak. We note that the oxygen mass measured here is the lower limit on the oxygen mass in the ejecta. The lower and upper limits of the O mass provided in the "O mass" column correspond to 4000 and 3400 K, respectively.

and τ is the *e*-folding timescale. We fix the CIGALE ionization parameter log $U_{\rm ion}$ as −2. This is used to calculate the nebular emission from the ionized gas in H II regions. We adopt a modified Calzetti et al. (2000) attenuation curve to model the dust attenuation. We include dust emission based on the Dale et al. (2014) dust templates. Further details on the different models can be found in Boquien et al. (2019). We generated 24,385,536 models based on the mentioned configuration, from which we chose the best fit using Bayesian inference. Table 9 lists the parameters used to generate the models, and Table 10 lists the best-fit parameters for all the host galaxies.

The hosts of all transients were detected in images of SDSS, Pan-STARRS, and the DESI Legacy Imaging Surveys. Figure 9 shows the *B*-band luminosities of the hosts for our sample. The entire distribution spans a wide range from $M_B \approx -15.7$ to -21.8 mag. This interval covers the range from $10^{-2}L_\star$ to $10L_\star$, where $L_\star$ is the knee of the *B*-band luminosity functions reported in Ilbert et al. (2005), covering the entire parameter space of star-forming galaxies. The majority of the hosts are found in galaxies between a few × 10^{-2} and a few $L^\star$. These host properties are identical to hosts of usual CCSNe. This is illustrated by the contours encircling 68%, 90%, and 95% of the PTF+iPTF CCSN sample (Schulze et al. 2021), which includes 888 objects from all major CCSN classes.

To compare the physical properties of the host galaxies, we present them in the mass–star formation rate (SFR) plane (Figure 10). The hosts are located in a narrow region of the parameter space that is occupied by a general population of star-forming galaxies, called the main sequence of star-forming galaxies (indicated by the gray shaded region; Elbaz et al. 2007). A small minority of our SNe occurred in galaxies that lie clearly above the galaxy main sequence and are experiencing a starburst. Like in Figure 9, we overlay the 68%, 90%, and 95% contours of the PTF CCSN host sample. The hosts of regular CCSNe occupy exactly the same parameter space, including the starburst regime (e.g., Taggart & Perley 2021). Most of the host galaxies are actively star-forming, which shows that the core-collapse Ca-rich sample is a different class from the usual Ca-rich sample, which are usually found in the outskirts of quenched galaxies. This is also evident from Figure 11, which shows that the projected physical offset distance for gap Ca-rich thermonuclear transients is systematically higher (*p*-value = 0.06 for a two-sided K-S test) than that of our Ca-rich Type IIb sample and the general core-collapse population (for the sample presented in De et al. 2020).

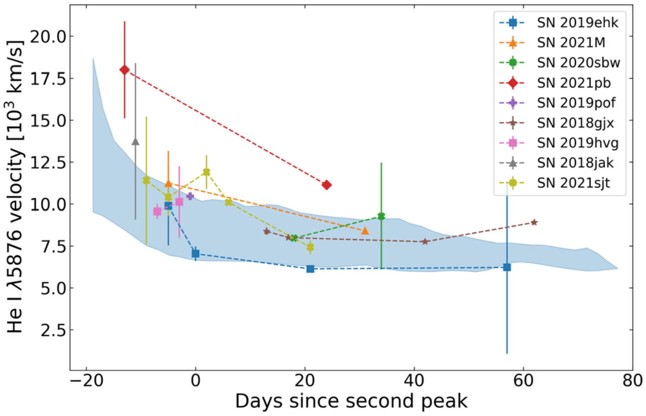

Figure 4. The expansion velocity of the He I line for each SN of our sample represented by the filled symbols. The blue shaded region shows the 1σ region of the ejecta velocity calculated for a sample of usual Type IIb SNe in Fremling et al. (2018).

4. Discussion

In this paper, we analyze the photometric and spectroscopic properties of the sample of a distinct class of Ca-rich Type IIb SNe. The sources in our sample are all CCSNe and not thermonuclear in origin. This is evident from the presence of photospheric hydrogen in the spectra (see Section 3.2), which suggests $M_{\rm H} \gtrsim 0.02$–$0.03\,M_\odot$ (Hachinger et al. 2012). The usual Ca-rich Type I events involve CO + He binary WDs progenitors, which are expected to be very deficient in hydrogen ($M_{\rm H} < 10^{-4}$ $M_\odot$; Podsiadlowski et al. 2003; Zenati et al. 2019). Hence, the formation pathway of our sample is distinct from the thermonuclear Ca-rich gap transients found in old environments. The host galaxy properties described in Section 3.5 are also consistent with those of the core-collapse population exploding in star-forming galaxies. The observed photospheric velocities, which are consistent with canonical SESNe, also rule out the fallback SN scenario, which has an expected velocity of ∼3000 km s^{-1} (Moriya et al. 2010). In this section, we discuss the constraints on the progenitors and implications on the progenitor channels for this class.

Table 5
Summary of the Best-fit Parameters Obtained from Shock-cooling Modeling of the First Peak

ZTF Source	$E_{\rm ext}$ (10^{50} erg)	$R_{\rm ext}$ ($R_\odot$)	$M_{\rm ext}$ ($10^{-2}\ M_\odot$)	$t_{\rm exp}$ (JD)
SN 2019ehk/ZTF19aatesgp	$3.95^{+0.34}_{-0.32}$	108^{+10}_{-9}	$20.26^{+0.99}_{-0.96}$	$2458602.08^{+0.01}_{-0.01}$
SN 2021M/ZTF21aaabwfu	$7.13^{+1.77}_{-1.91}$	34^{+11}_{-6}	$32.38^{+3.90}_{-4.66}$	$2459213.53^{+0.05}_{-0.02}$
SN 2020sbw/ZTF20abwzqzo	$0.15^{+0.06}_{-0.03}$	2938^{+1103}_{-1334}	$1.68^{+0.34}_{-0.16}$	$2459086.57^{+0.07}_{-0.08}$
SN 2021pb/ZTF21aabxjqr	$4.57^{+0.84}_{-0.71}$	118^{+19}_{-16}	$30.97^{+2.63}_{-2.45}$	$2459218.01^{+0.02}_{-0.01}$
SN 2019pof/ZTF19abxtcio	$0.10^{+0.06}_{-0.03}$	368^{+188}_{-149}	$8.52^{+1.77}_{-1.33}$	$2458730.35^{+0.48}_{-0.25}$
SN 2018gjx/ZTF18abwkrbl	$14.08^{+0.40}_{-0.41}$	47^{+1}_{-1}	$41.00^{+0.86}_{-0.88}$	$2458376.34^{+0.01}_{-0.01}$
SN 2019hvg/ZTF19abacxod	$1.85^{+0.34}_{-0.30}$	121^{+22}_{-18}	$23.36^{+2.05}_{-1.97}$	$2458651.03^{+0.04}_{-0.02}$
SN 2018jak/ZTF18acqxyiq	$9.92^{+0.06}_{-0.12}$	234^{+7}_{-7}	$54.19^{+1.19}_{-1.15}$	$2458442.50^{+0.01}_{-0.01}$
SN 2021sjt/ZTF21abjyiiw	$0.07^{+0.01}_{-0.01}$	1946^{+805}_{-504}	$2.47^{+0.26}_{-0.26}$	$2459400.70^{+0.03}_{-0.01}$

Table 6
Summary of the Best-fit Physical Parameters Obtained by Radioactive Decay Modeling of the Second Peak of the SNe in Our Sample

Source	$M_{\rm Ni-Ar}$[a] ($M_\odot$)	$M_{\rm Ni-KK}$ ($M_\odot$)	$M_{\rm ej-Ar}$ ($M_\odot$)	$M_{\rm ej-KK}$ ($M_\odot$)	$E_{\rm kin}$ (10^{51} erg)	t_0 (days)
SN 2019ehk/ZTF19aatesgp	0.02–0.08	0.08	$0.35^{+0.01}_{-0.01}$	0.32	$0.21^{+0.01}_{-0.01}$	$37.79^{+0.98}_{-0.96}$
SN 2021M/ZTF21aaabwfu	0.04–0.13	0.14	$1.05^{+0.64}_{-0.54}$	0.79	$0.76^{+0.46}_{-0.39}$	$52.83^{+2.86}_{-2.76}$
SN 2020sbw/ZTF20abwzqzo	0.02–0.13	0.14	$0.77^{+0.09}_{-0.07}$	0.57	$0.29^{+0.04}_{-0.03}$	$59.76^{+1.57}_{-1.60}$
SN 2021pb/ZTF21aabxjqr	0.10–0.12	0.13	$3.57^{+2.74}_{-0.58}$	2.21	$5.46^{+4.19}_{-0.89}$	$56.84^{+29.20}_{-29.00}$
SN 2019pof/ZTF19abxtcio	0.01–0.03	0.04	$0.77^{+0.37}_{-0.14}$	0.59	$0.46^{+0.22}_{-0.08}$	$40.17^{+1.39}_{-1.44}$
SN 2018gjx/ZTF18abwkrbl	0.04–0.05	0.05	$0.20^{+0.02}_{-0.02}$	0.19	$0.08^{+0.00}_{-0.00}$	$59.32^{+1.18}_{-1.13}$
SN 2019hvg/ZTF19abacxod	0.02–0.13	0.15	$1.15^{+0.08}_{-0.07}$	0.81	$0.56^{+0.04}_{-0.03}$	$47.30^{+3.76}_{-2.90}$
SN 2018jak/ZTF18acqxyiq	0.03–0.12	0.11	$0.72^{+0.04}_{-0.04}$	0.62	$0.73^{+0.04}_{-0.04}$	$93.83^{+4.40}_{-6.61}$
SN 2021sjt/ZTF21abjyiiw	0.01–0.05	0.05	$1.15^{+0.03}_{-0.03}$	0.83	$0.83^{+0.02}_{-0.02}$	$50.23^{+0.77}_{-0.74}$

Note. The "Ar" subscript refers to the Arnett et al. (1989) model, while the "KK" subscript refers to the Khatami & Kasen (2019) model.

[a] Lower limit is calculated by assuming no host extinction.

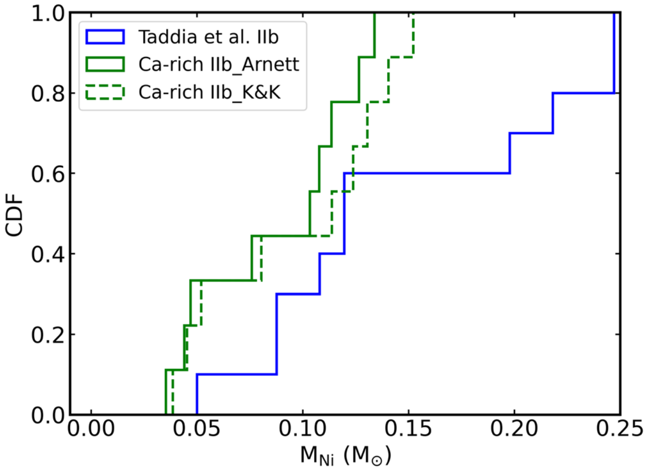

Figure 5. ^{56}Ni mass distribution for our sample of SNe IIb compared to the SN IIb population presented in Taddia et al. (2018).

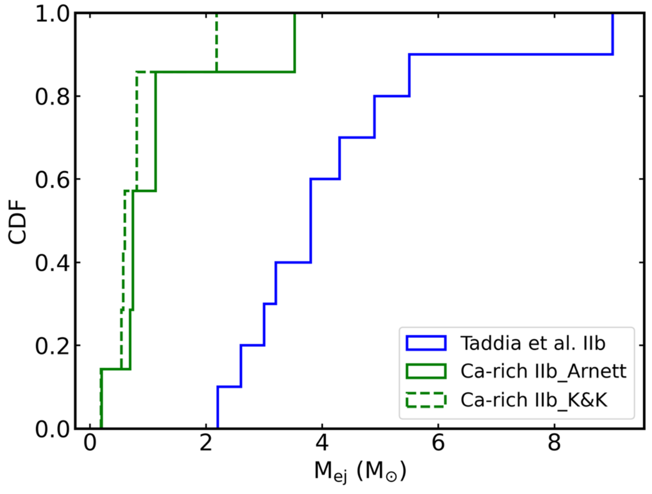

Figure 6. Ejecta mass distribution for our sample of SNe IIb compared to the SN IIb population presented in Taddia et al. (2018).

4.1. Constraints on Progenitor Mass

4.1.1. Constraining Progenitor Mass Using Nebular Spectra

For all the SNe in our sample, we have at least one nebular spectrum obtained using the Low Resolution Imaging Spectrograph (LRIS) on the Keck I telescope. We calculate the [Ca II]/[O I] flux ratio and the [O I] luminosity using the procedure described in Section 3.3 (see Table 4). Next, we use the measured [O I] luminosity to calculate the oxygen abundance and subsequently the progenitor mass. We use the following analytical relation provided in Uomoto (1986) to calculate the minimum O mass required for a given [O I] luminosity: $M_{\rm O} = 10^8\ (L[{\rm O\ I}]/4\pi D_{\rm cm}^2)\ D_{\rm Mpc}^2\ \exp(2.28/T\,(10^4{\rm K}))\ M_\odot$, where L[O I] is the luminosity in erg s^{-1} of [O I] $\lambda\lambda$6300, 6364. The analytical formula is valid in the high-density limit where the electron density is above the [O I] critical density ($\sim 7 \times 10^5$ cm^{-3}), and it is estimated to hold in our case for estimated ejecta mass in the range of 0.5–2 $M_\odot$. We use typical

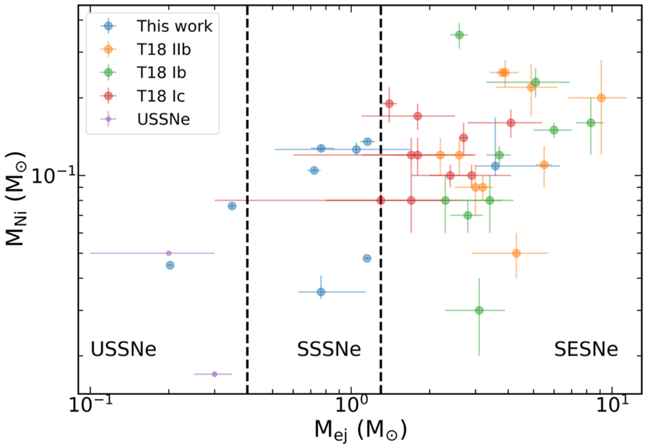

Figure 7. Comparison of the ^{56}Ni mass and the ejecta mass based on the Arnett fit for our sample and usual stripped-envelope Type IIb SNe from Taddia et al. (2018) and USSNe from De et al. (2018) and Yao et al. (2020). We find that the SSSNe in our sample are a transient class between the USSNe and the usual SESNe (rough boundaries indicated by the vertical dashed lines). We also note that there is a region in the parameter space that is unoccupied by the SESN population.

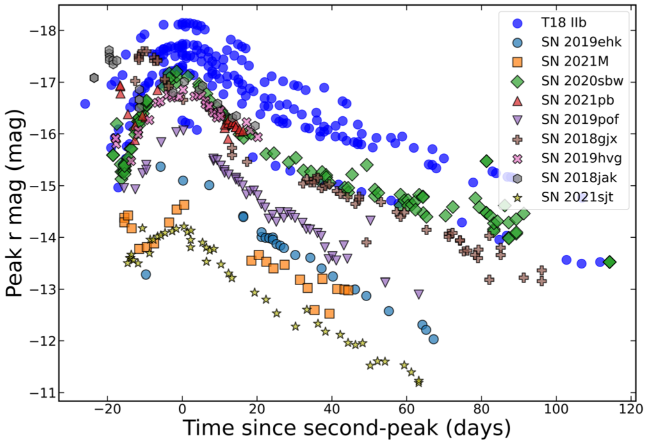

Figure 8. Comparison of the light curves of the Ca-rich Type IIb SNe in our sample (in filled shapes of different types) with canonical Type IIb SN light curves from Taddia et al. (2018; in blue circles). The *y*-axis shows the absolute magnitude (mag), with galactic extinction correction. The *x*-axis shows the number of rest-frame days since the second peak.

temperature values estimated from the [O I] emission in other CCSNe of ≈3500–4000 K (Sollerman et al. 1998; Elmhamdi 2011) to get lower limits on the O mass in the range of ≈0.005–0.1 $M_\odot$. The lower and upper limits of the O mass provided in Table 4 correspond to 4000 and 3400 K, respectively.

We compare the observed [O I] luminosity and measured oxygen mass lower limits with theoretical models to constrain the progenitor mass. Jerkstrand et al. (2015) presented the dependence of [O I] luminosity on progenitor mass using detailed nebular-phase models of SESNe (see Figure 12). We see that the nebular models of progenitors with mass $>12\,M_\odot$ consistently overestimate the [O I] luminosity. This suggests a much lower progenitor core mass for our sample. In Figure 13, we plot model tracks showing the steep dependence of O mass on the initial ZAMS mass obtained from canonical core-collapse nebular models (taken from Nomoto et al. 1997; Rauscher et al. 2002; Limongi & Chieffi 2003). We consistently find that the ZAMS mass required to explain the observed O mass lower limits of our sample can be less than $12\,M_\odot$.

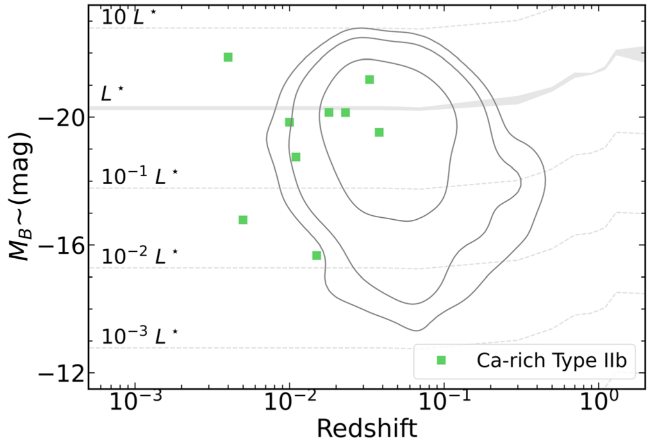

Figure 9. The absolute *B*-band magnitude of CCSN host galaxies as a function of redshift. Our hosts are found in the least luminous ($10^{-3}L^\star$) to the most luminous star-forming galaxies ($\lesssim 5L^\star$) ($L^\star$ is the characteristic luminosity of the *B*-band luminosity function of star-forming galaxies). Most Ca-rich IIb hosts have luminosities of 10^{-2} to a few $L^\star$, similar to regular CCSNe (indicated by the contours encircling 68%, 90%, and 95% of the PTF+iPTF CCSN sample; Schulze et al. 2021). We also indicate the $L^\star$ presented in Faber et al. (2007) and multiples of it in gray.

Dessart et al. (2021) presented a set of 1D non−local thermodynamic equilibrium radiative transfer calculations for nebular-phase stripped SNe. In models from He stars with an initial mass $>6\,M_\odot$, they find that the [O I] line strength is of comparable or greater strength than [Ca II] lines. The initial helium star mass reflects the mass of the helium core at the time of central helium ignition. In contrast, they show that models from lower-mass He stars exhibit a weak [O I] and strong [Ca II]. The high [Ca II]/[O I] flux ratio we observe for our sample is thus consistent with low initial He-star mass. Figure 13 compares the measured O mass lower limits for our sample with the synthesized O mass from the He-star progenitor models that assume an evolution in a binary system (Dessart et al. 2021) and with those arising from single-star models (Sukhbold et al. 2016). In both the binary and single-star systems, core collapse is reached with a residual H-rich envelope. Again, we find that the observed oxygen yield is consistent with the lowest ZAMS mass ($<12\,M_\odot$) models for stripped He stars with initial mass less than $\sim 3\,M_\odot$. We use the relations in Woosley & Heger (2015) to get the ZAMS mass from the initial He-star mass.

To compare with such low ZAMS masses, we use estimates of the O synthesized for the case of the highly stripped He cores of USSNe. These are modeled as relatively low mass He stars ($<3.5\,M_\odot$) that are stripped down by a close binary companion, leaving behind CO cores of $\approx 1.45-1.6\,M_\odot$ at the time of explosion (Tauris et al. 2015). We note that the CO core mass is a good tracer of the progenitor ZAMS, as it is insensitive to the binary stripping that occurs in the very late stages of stellar evolution (Fransson & Chevalier 1989; Jerkstrand et al. 2014, 2015). We find that the O yields for such strongly stripped stars with low CO core mass are comparable to the low O yield of sources in our sample (see Figures 12 and 13).

We caution that we assume that the radioactive power deposited in the O-rich shells of the ejecta is released via cooling in the [O I] lines. We note that this is dependent on the

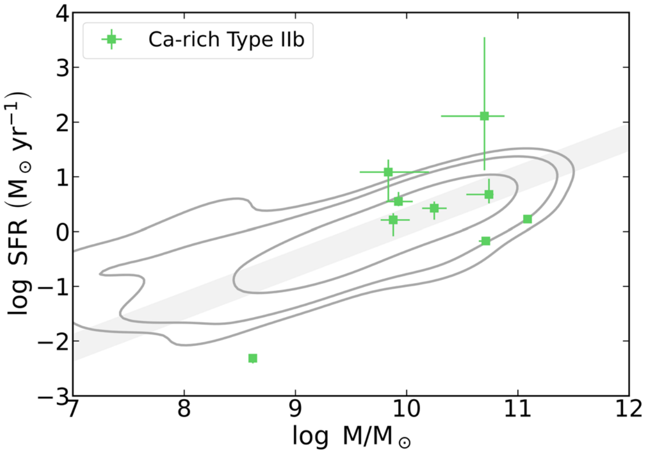

Figure 10. The host population in the mass−SFR plane. All sources exploded in star-forming galaxies. This is illustrated by their location with respect to the main sequence of star-forming galaxies (gray shaded region). The majority of hosts also have properties consistent with those of CCSNe from the PTF+iPTF surveys (gray contours indicate the region encircling 68%, 90%, and 95% of the sample; Schulze et al. 2021).

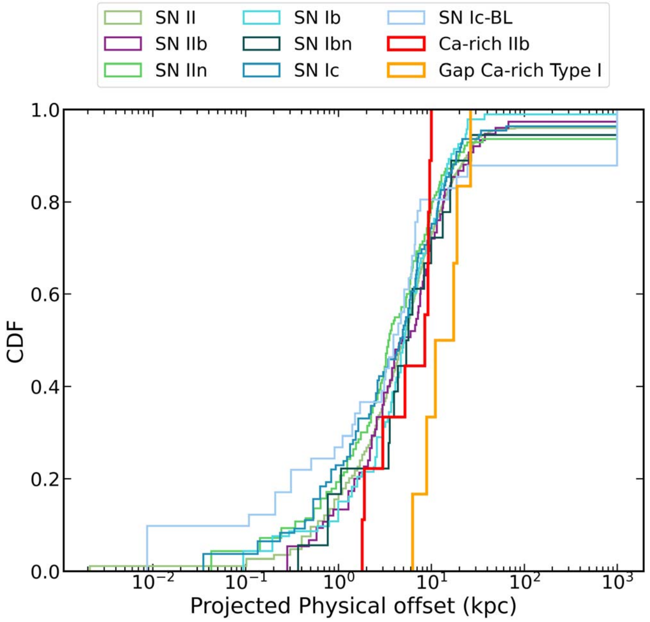

Figure 11. The projected physical offset distribution of all the SNe in our sample compared with the distribution for other types of SNe measured in De et al. (2020). We note that there is a distinct offset from the gap Ca-rich Type I SNe, known to occur in quenched environments.

presence of impurity species, e.g., Dessart & Hillier (2020) showed that even a small amount of Ca mixed into O-rich regions can dramatically weaken the cooling by [O I]. However, it has been shown that mixing is not significant for CCSNe. Detailed modeling of CCSNe has shown that [O I] emission arises from the outer O-rich layers produced during the hydrostatic burning phase, while the [Ca II] line is the primary coolant in the Si-rich layers (Jerkstrand et al. 2015; Dessart & Hillier 2020). In addition, Polin et al. (2021) show that pollution of ^{40}Ca even at the 1% level will cause a nebular region to completely cool through [Ca II] emission, suggesting that if these ejecta regions were mixed, it would be difficult to see any contribution from [O I].

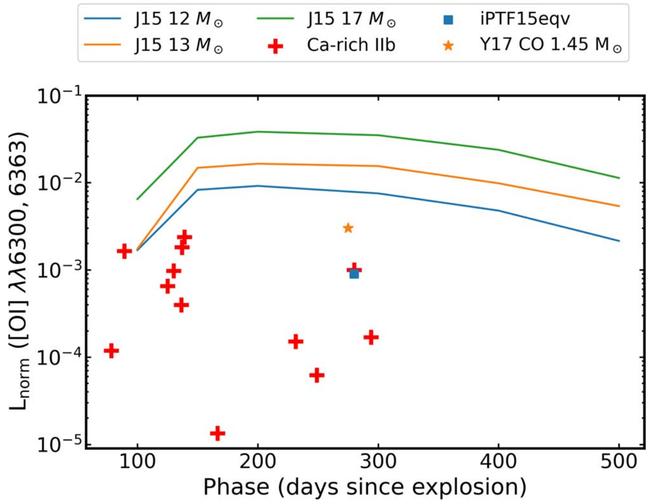

Figure 12. The red plus signs show the [O I] luminosities calculated from the nebular spectra for the Ca-rich Type IIb sample. The luminosity is normalized to the ^{56}Co decay energy. We compare these to models of stripped-envelope CCSNe from Jerkstrand et al. (2015). We also show the measured normalized [O I] luminosities from the nucleosynthesis calculations of Yoshida et al. (2017) and the Ca-rich Type IIb iPTF 15eqv.

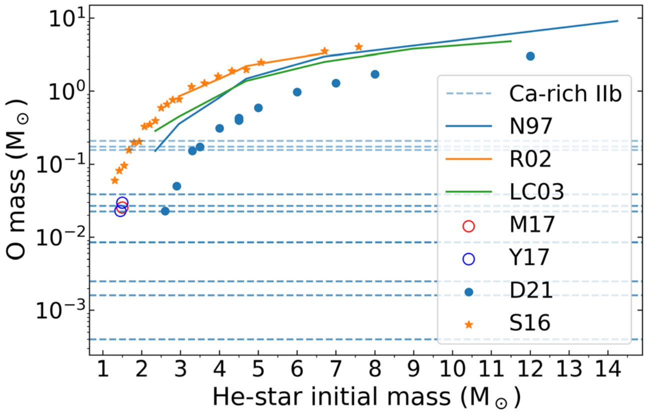

Figure 13. The measured O mass lower limits are shown with the horizontal dashed lines. The O yields for the ejecta arising from the He-star progenitor models, which assume an evolution in a binary system (Dessart et al. 2021), are shown with filled blue circles, and those arising from the single-star models (Sukhbold et al. 2016) are shown with filled orange stars. We also plot the O mass for nucleosynthetic models of higher-ZAMS stars (Nomoto et al. 1997; Rauscher et al. 2002; Limongi & Chieffi 2003) and for lower-ZAMS stars from USSN models of Yoshida et al. (2017) and Moriya et al. (2017).

4.1.2. Constraining Progenitor Mass Using Light Curves

We fit the double-peaked light curves of the SN sample using the Piro et al. (2021) and Arnett et al. (1989) models as described in Section 3.4.2. The best-fit parameters of the shock-cooling breakout peak and the radioactive-powered peak, such as $M_{\rm Ni}$, $M_{\rm ej}$, $E_{\rm kin}$, and $R_{\rm env}$, are tabulated in Tables 5 and 6.

In order to constrain the progenitor properties, we plot the evolutionary track of the predicted ejecta properties as a function of He-star initial mass or initial ZAMS mass from Dessart et al. (2021). They use He-star models of Woosley (2019) with initial He-star masses spanning the range from 2.6 to 13 $M_\odot$ that were evolved to the onset of core collapse. The ejecta properties shown by the filled circles in Figure 14 are obtained after performing nebular-phase NLTE steady-state and time-dependent radiative transfer calculations based on prescribed He-star explosion models of Ertl et al. (2020).

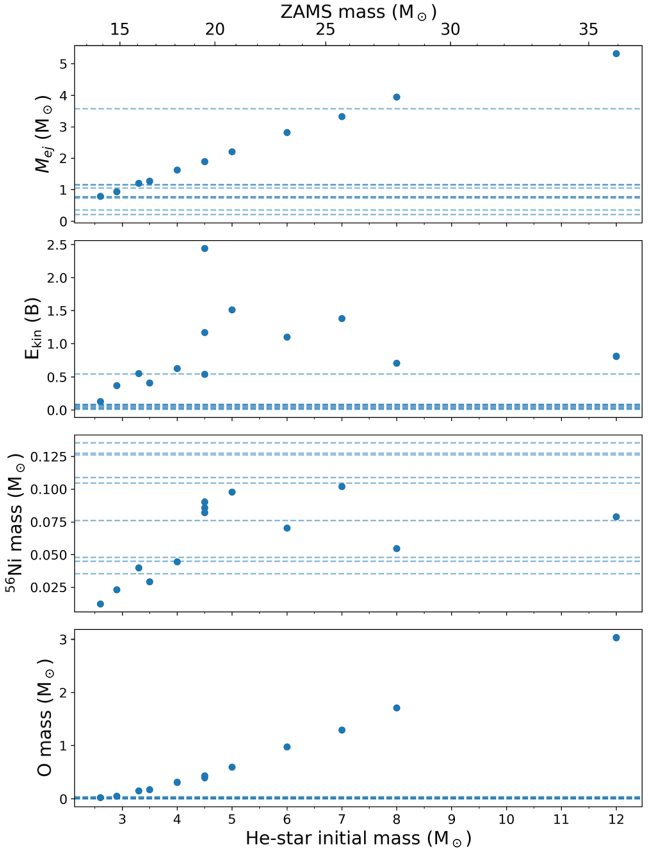

Figure 14. Comparison of the ejecta properties we observe (horizontal dashed lines) for our sample with that for the explosion models based on He stars evolved with the nominal mass-loss rate from Dessart et al. (2021; filled circles). From top to bottom, we show the ejecta mass $M_{\rm ej}$, ejecta kinetic energy $E_{\rm kin}$, ^{56}Ni mass, and oxygen yield.

Depending on the adopted pre-SN mass-loss recipe, they give rise to ejecta masses between 0.79 and 5.32 $M_\odot$. The ejecta mass values we obtain are consistent with those predicted for the lower end of the He-star mass stars ($<12\ M_\odot$). They report that the lower-mass progenitors with initial He-star mass of $\approx 2.6\ M_\odot$, calibration to the Crab, and realistic 10 $M_\odot$ single-star simulations imply an explosion energy of $\sim 10^{51}$ erg. It can be seen from Figure 14 that the kinetic energy of our sample is consistently lower than that predicted for ZAMS stars of $\sim 12\ M_\odot$. We note that most SNe in our sample have low ejecta mass while having high Ni mass. This could be due to an enhanced mass-loss rate of the pre-SN He star. Dessart et al. (2021) found that there is a systematic increase in the ^{56}Ni production by a few factors depending on the mass-loss rate and the initial mass. The high Ni mass makes an electron-capture core-collapse scenario unlikely, as simulations consistently predict an upper limit of $\sim 10^{-2}\ M_\odot$, which is an order of magnitude lower than those observed for our sample.

Next, we compare the observed explosion energy values with predictions from state-of-the-art 2D and 3D CCSN simulations. Burrows et al. (2019) use the CCSN code FORNAX to simulate the behavior of CCSNe at the lower-mass end (9, 10, 11, 12, and 13 $M_\odot$) in three spatial directions, while Burrows et al. (2020) conduct 19 3D CCSN simulations spanning a wide range of progenitor masses from 9 to 60 $M_\odot$. Neutrino heating, turbulence behind the stalled shock, and energy transfer due to neutrino−matter absorption and neutrino−matter scattering, among other factors, were conducive for the explosion of these low-mass progenitors. They consistently find that the lower-mass massive-star progenitors in the 9−12 $M_\odot$ range experience lower-energy explosions, while the higher-mass massive stars experience higher-energy explosions. In Figure 15, we compare the predicted energy values from Burrows et al. (2019) and Burrows & Vartanyan (2021) with the observed values for our sample. We find that the explosion energy values ($\sim 10^{50}$ erg) we obtain are roughly consistent with the 2D models and completely consistent with the 3D SN simulations for the $\approx$9–12 $M_\odot$ progenitors. We note that the explosion energy predicted from these models is defined as sum of the gravitational, kinetic, thermal, and recombination energies of the ejecta and thus should be treated as an upper limit to the explosion kinetic energy. The models also mention a gap in explodability for 13 $M_\odot$ in Burrows et al. (2019), potentially due to shallow mass density and subtle Si/O interface, which can be explored with a larger sample of well-constrained low-mass CCSNe.

It is has been shown from simulations that progenitors of SESNe with initial masses below 10 $M_\odot$ expand to large radii (up to 100 $R_\odot$), while more massive progenitors stay compact (e.g., Laplace et al. 2020). Only progenitors with low initial masses in the 8−9 $M_\odot$ range can swell enough for renewed interaction with their companion. This is consistent with the envelope radii of our sample, with values lying in the 100−1000 $R_\odot$ range. The extent of expansion of a stripped star is critical to understand their fate as the progenitors of CCSNe. The large radii of stripped stars imply that they can potentially fill their Roche lobe again and undergo another phase of mass transfer (Dewi et al. 2002; Dewi & Pols 2003). Additional phases of mass transfer can produce stars with very low envelope masses, possibly explaining the low ejecta mass we observe for our sample.

4.2. Strongly Stripped Envelope SNe

As discussed in Section 4.1.2, the ejecta masses observed are consistent with theoretical predictions for stripped He stars with initial mass less than 3 $M_\odot$. These occur in tight binaries where a helium star transfers mass to a small companion. The core collapse of such stellar cores with a small envelope gives rise to low ejecta mass explosions. One way to form such progenitor stars in the stellar evolution theory is through the USSN scenario (Tauris et al. 2013, 2015). These explosions are one of two channels to form double NS binaries that are compact enough to merge within a Hubble time owing to gravitational-wave radiation.

Nakaoka et al. (2021) suggested that the Ca-rich Type IIb SN 2019ehk originated in a USSN. Low-mass progenitors of stripped CCSNe can retain a range of H and He masses depending on the nature of the companion and the initial binary period (Yoon et al. 2010; Zapartas et al. 2017; Laplace et al. 2020). The presence of hydrogen represents a less extreme case of a "strongly stripped SN" (ejecta mass $\approx 0.6\ M_\odot$) from a low-mass (ZAMS $\approx$9–12 $M_\odot$) progenitor that lost nearly all of its H envelope to stripping in a relatively compact orbit (orbital period ∼10 days). This is a transition class between the USSNe and the usual SESNe (see Figure 7). The progenitor could be stripped by a main-sequence companion and resulted in the formation of a compact NS−main sequence binary. Such binaries have been suggested to be progenitors of NS−WD systems that could merge within a Hubble time and be detectable with LISA (Toonen et al. 2018).

We compare our estimates of the O yields with those predicted for USSNe (Tauris et al. 2013). We use the nucleosynthetic yields from Moriya et al. (2017) and Yoshida et al. (2017) to estimate the [O I] luminosity in the nebular phase for low-mass CO cores of 1.45–1.5 $M_\odot$, under different assumptions of the explosion energy and ejecta mass. Figure 12 shows that the upper limits on the [O I] luminosity for the low-mass CO core models are similar to the low [O I] luminosity measured for our sample. In addition, we find that the O masses estimated in the context of USSNe are consistent with the range estimated for our sample (see Section 4.1.1),

Ca-rich spectra strengthen the case for a strongly stripped envelope scenario. Explosion of low-mass He-star progenitors can explain the dominance of calcium emissions over the oxygen emissions (i.e., deficiency in the oxygen emissions) in the nebular spectra (Kawabata et al. 2010; Maeda et al. 2007; Fang et al. 2019). In addition, the rapid evolution seen for our sample is a natural consequence from such a scenario. Such low-mass progenitor explosions are a boundary between the SN explosion (by either a Fe core collapse or ONeMg core electron capture) and WD formation and predict small ejecta mass, i.e., $<0.5\ M_\odot$ (Tauris et al. 2013; Moriya et al. 2017). These features are consistent with the observational properties of the Ca-rich Type IIb transients.

Thus, we conclude that the ejecta properties of our sample are generally consistent with the expectations for a low-mass ($<2\ M_\odot$) He (or C+O) star explosion corresponding to ZAMS mass of 8–12 $M_\odot$, which defines a boundary between the CCSN explosion and a WD formation. Assuming a residual H mass of $\sim$0.1 $M_\odot$, the inferred ejecta mass of our sample of $<0.6\ M_\odot$ is consistent with a final CO core mass of $\approx$1.45–1.5 $M_\odot$ that collapses to form a $\approx$1.3 $M_\odot$ NS and ejects $\approx$0.5 $M_\odot$ of material. The inferred ejecta mass points to a class of SSSNe that are potential progenitors of NS–WD systems.

4.3. Rate Estimation

For this work, since all our sources were detected in the BTS, we follow the rate estimation analysis adopted by Perley et al. (2020). We discuss the procedure in brief below.

In the case of an ideal survey that is able to scan the entire sky to a given magnitude limit $m_{\rm lim}$, the volumetric rate can be estimated using

$$R = \frac{1}{t}\sum_{i=1}^{N}\frac{1}{\left(\frac{4\pi}{3}D^3_{{\rm max},i}\right)}, \tag{1}$$

where t is the duration of the survey and $D_{{\rm max},i}$ is the distance out to which the ith transient can be detected above $m_{\rm lim}$ at peak light in the absence of extinction, given its peak absolute magnitude M_i. However, for practical surveys, there are multiple loss factors one needs to take into account. For this work, we follow the revised equation adopted by Perley et al. (2020):

$$R = \frac{1}{t}\sum_{i=1}^{N}\frac{1}{\left(\frac{4\pi}{3}D^3_{{\rm max},i}\right) f_{\rm sky}\, f_{\rm ext}\, f_{\rm rec}\, f_{{\rm cl},i}}. \tag{2}$$

The description of the loss factors and their values used are listed below.

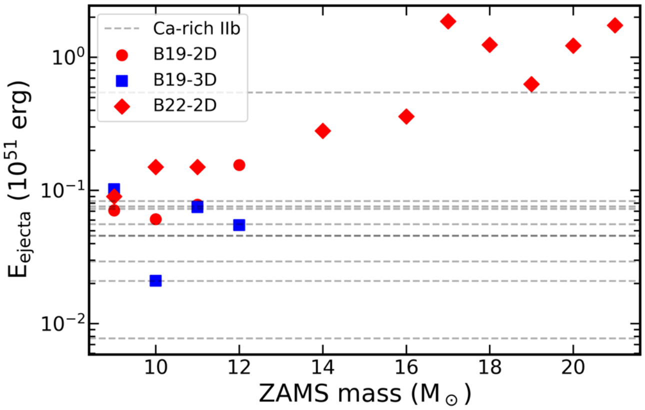

Figure 15. Comparison of the observed explosion energy values with predictions from Burrows et al. (2019; B19) and Burrows & Vartanyan (2021; B22). They use the CCSN code FORNAX to perform 2D and 3D CCSN simulations for a range of progenitor masses. See Section 4.1.2 for details.

1. $f_{\rm sky}$ is the average active survey footprint expressed as a fraction of the full sky. We use $f_{\rm sky} = 0.35$, based on the average active area of the BTS of $\sim$14,400 deg^2.
2. $f_{\rm ext}$ is the average reduction in effective survey volume due to Galactic extinction. We use $f_{\rm ext} = 0.82$, calculated by averaging the reduction in volume associated with the extinction toward each separate ZTF field. We do not correct for host galaxy extinction.
3. $f_{\rm rec}$ is the average recovery efficiency for a detectable transient within the survey footprint: the probability that it is found and included in the sample. We use $f_{\rm rec} = 0.60$. This was measured by calculating the fraction of all events classified as SNe Ia that passed the quality cuts of the ZTF survey.
4. $f_{{\rm cl},i}$ is the classification efficiency, which may depend on apparent magnitude. We use $f_{\rm cl} = 1.0$ if $m < 17.2$ mag and $f_{\rm cl} = 0.9$ at $m = 18.5$ mag, with a linear decline in between.

Refer to Perley et al. (2020) for further details on the calculation of the loss parameters. The sample as presented in this paper spans $t = 3.5$ yr of ZTF. We had around 94 sources classified as Type IIb as part of the BTS and the CLU survey, out of which we have good-quality nebular spectra for 29 Type IIb sources. We use $H_0 = 70$ km s^{-1}Mpc^{-1}. Based on these assumptions and the analysis adopted by Perley et al. (2020), we get a rate of $(5.1^{+6.6}_{-4.5}) \times 10^3$ Gpc^{-3}yr^{-1}. This is $\approx 6^{+12}_{-5}\%$ of CCSNe and $\approx 22^{+25}_{-19}\%$ of SNe Ia assuming a CCSN rate of $(7.7^{+6.6}_{-4.5}) \times 10^4$ Gpc^{-3}yr^{-1} and an SN Ia rate of $(2.35 \pm 0.24) \times 10^4$ Gpc^{-3} yr^{-1} calculated using the same procedure. As per present classifications, this is $\approx 22\% \pm 6\%$ of all SESNe and $\approx 44\% \pm 31\%$ of Type IIb SNe. We note that the rates are based on the present classification status. In addition, since these events have low luminosity and are low in number, the associated errors are high. We leave a more accurate rate estimate using a larger sample size and more complete nebular follow-up for future work.

NS–WD merger rates are predicted to be in the range of 3%–15% of the Type Ia SN rate (Toonen et al. 2018). The corresponding rates are consistent with that obtained for the Ca-rich Type IIb sample within the large errors, at the low end of the relative rate estimate. In addition, the delay time distribution suggests that these mergers are most likely to be found in star-forming galaxies, consistent with the host galaxy properties of our sample.

5. Conclusion

We examined the various photometric and spectroscopic properties of the objects in our sample of Ca-rich Type IIb SNe. We find that the observed properties of our sample suggest a class of SSSNe that form a transition class between the usual SESN and USSN groups. The key takeaways of the paper are as follows:

1. SSSNe are a class of CCSNe that have ejecta mass less than $\sim 1\ M_\odot$ but show hydrogen in the ejecta. They have been classified as Type IIb SNe based on the photospheric spectra. The SNe in our sample also show a high [Ca II]/[O I] flux ratio ($\geqslant 2$) in the nebular spectra. Observed properties suggest that the progenitor could be stripped by a main-sequence companion and may result in the formation of a compact NS−main sequence binary. Such binaries have been suggested to be progenitors of NS−WD systems that could merge within a Hubble time and be detectable with LISA.
2. The ejecta and spectroscopic properties of the class are generally consistent with the expectations for a low-mass ($<3\ M_\odot$) He-star explosion corresponding to a ZAMS mass less than 12 $M_\odot$. From the low [O I] $\lambda\lambda$6300, 6364 luminosity in the nebular-phase spectra, we find that the estimated progenitor oxygen mass lower limits for our sample are in the range ≈ 0.005–$0.1\ M_\odot$. For CCSN models to reproduce our inferred oxygen mass, we infer that the ZAMS mass is less than 12 $M_\odot$. Other measured properties, such as the [Ca II]/[O I] ratio, ejecta mass, kinetic energy, and envelope radius, are also consistent with the 8−12 $M_\odot$ progenitor mass scenario.
3. The presence of photospheric hydrogen suggests $M_{\rm H} \gtrsim 0.02$–$0.03\ M_\odot$ (Hachinger et al. 2012). The proposed explosion mechanism for the usual Ca-rich Type I events involves CO + He binary WD progenitors. However, they are expected to be very deficient in hydrogen ($M_{\rm H} < 10^{-4}\ M_\odot$). In addition, the host galaxies of the SSSN class are consistent with star-forming galaxies, as they lie in the galaxy main sequence of the mass−SFR plane and have a luminosity range consistent with the hosts for the general Type IIb SN population. Hence, our sample is distinct from the thermonuclear Ca-rich gap transients found in old environments.

Thus, we present a class of SNe that lie in the low-mass end of CCSNe and are a transition class between USSNe and the usual SESNe. Observational constraints for such low-mass He stars are missing in the literature. This sample provides an opportunity to understand the low-mass He-star evolution and the extent of binary stripping and would help in developing theoretical models including nebular spectra for this low mass range. Discovery and follow-up of more members of this class will help obtain a stricter constraint on the rates of these events.

Acknowledgments

We thank Adam Burrows for valuable comments on the manuscript. We thank the anonymous referee for the valuable comments that significantly improved the quality of the paper. Based on observations obtained with the Samuel Oschin Telescope 48-inch and the 60-inch Telescope at the Palomar Observatory as part of the Zwicky Transient Facility project. ZTF is supported by the National Science Foundation under grant No. AST-2034437 and a collaboration including Caltech, IPAC, the Weizmann Institute of Science, the Oskar Klein Center at Stockholm University, the University of Maryland, Deutsches Elektronen-Synchrotron and Humboldt University, the TANGO Consortium of Taiwan, the University of Wisconsin at Milwaukee, Trinity College Dublin, Lawrence Livermore National Laboratories, IN2P3, France, the University of Warwick, the University of Bochum, and Northwestern University. Operations are conducted by COO, IPAC, and UW.

SED Machine is based on work supported by the National Science Foundation under grant No. 1106171.

The ZTF forced-photometry service was funded under the Heising-Simons Foundation grant No. 12540303 (PI: Graham).

The GROWTH Marshal was supported by the GROWTH project funded by the National Science Foundation under grant No. 1545949.

The data presented here were obtained in part with ALFOSC, which is provided by the Instituto de Astrofisica de Andalucia (IAA) under a joint agreement with the University of Copenhagen and NOT.

The Liverpool Telescope is operated on the island of La Palma by Liverpool John Moores University in the Spanish Observatorio del Roque de los Muchachos of the Instituto de Astrofisica de Canarias with financial support from the UK Science and Technology Facilities Council. Based on observations made with the Italian Telescopio Nazionale Galileo (TNG) operated on the island of La Palma by the Fundación Galileo Galilei of the INAF (Istituto Nazionale di Astrofisica) at the Spanish Observatorio del Roque de los Muchachos of the Instituto de Astrofisica de Canarias.

The W. M. Keck Observatory is operated as a scientific partnership among the California Institute of Technology, the University of California, and the National Aeronautics and Space Administration. The Observatory was made possible by the generous financial support of the W. M. Keck Foundation. The authors wish to recognize and acknowledge the very significant cultural role and reverence that the summit of Maunakea has always had within the indigenous Hawaiian community. We are most fortunate to have the opportunity to conduct observations from this mountain. The `ztfquery` code was funded by the European Research Council (ERC) under the European Union's Horizon 2020 research and innovation program (grant agreement No. 759194 – USNAC; PI: Rigault).

S.S. acknowledges support from the G.R.E.A.T. research environment, funded by *Vetenskapsrådet*, the Swedish Research Council, project No. 2016-06012.

Data Availability

All the photometric and spectroscopic data used in this work can be found here.

The optical photometry and spectroscopy will also be made public through WISeREP, the Weizmann Interactive Supernova Data Repository (Yaron & Gal-Yam 2012).

Appendix A
Color Evolution

We show the color evolution of our objects compared to the Type IIb SNe sample of Taddia et al. (2018) in Figure 16 after extinction correction.

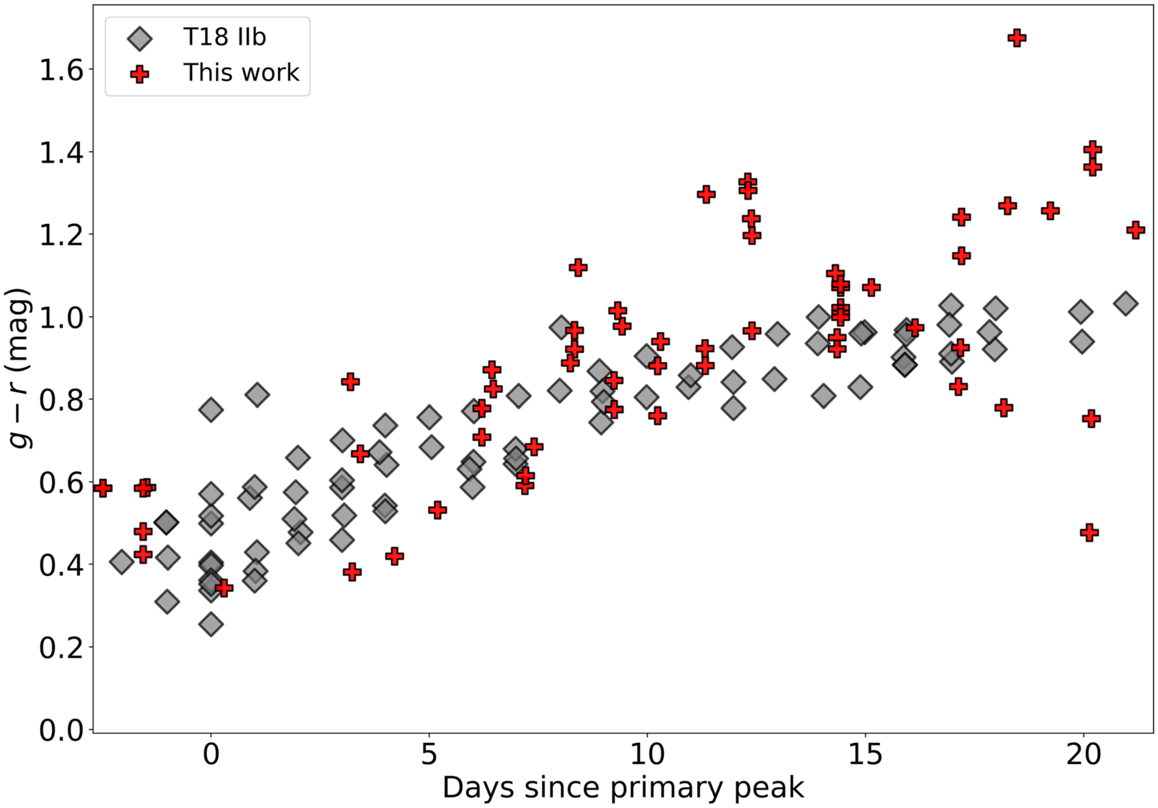

Figure 16. The $g - r$ color evolution of the SNe in our sample (red plus signs), compared to the Type IIb SN sample of Taddia et al. (2018; gray diamonds).

Appendix B
Nebular Spectra

The full wavelength range nebular spectra are shown in Figure 17. The phase of the spectra is measured as the number of rest-frame days since the second peak.

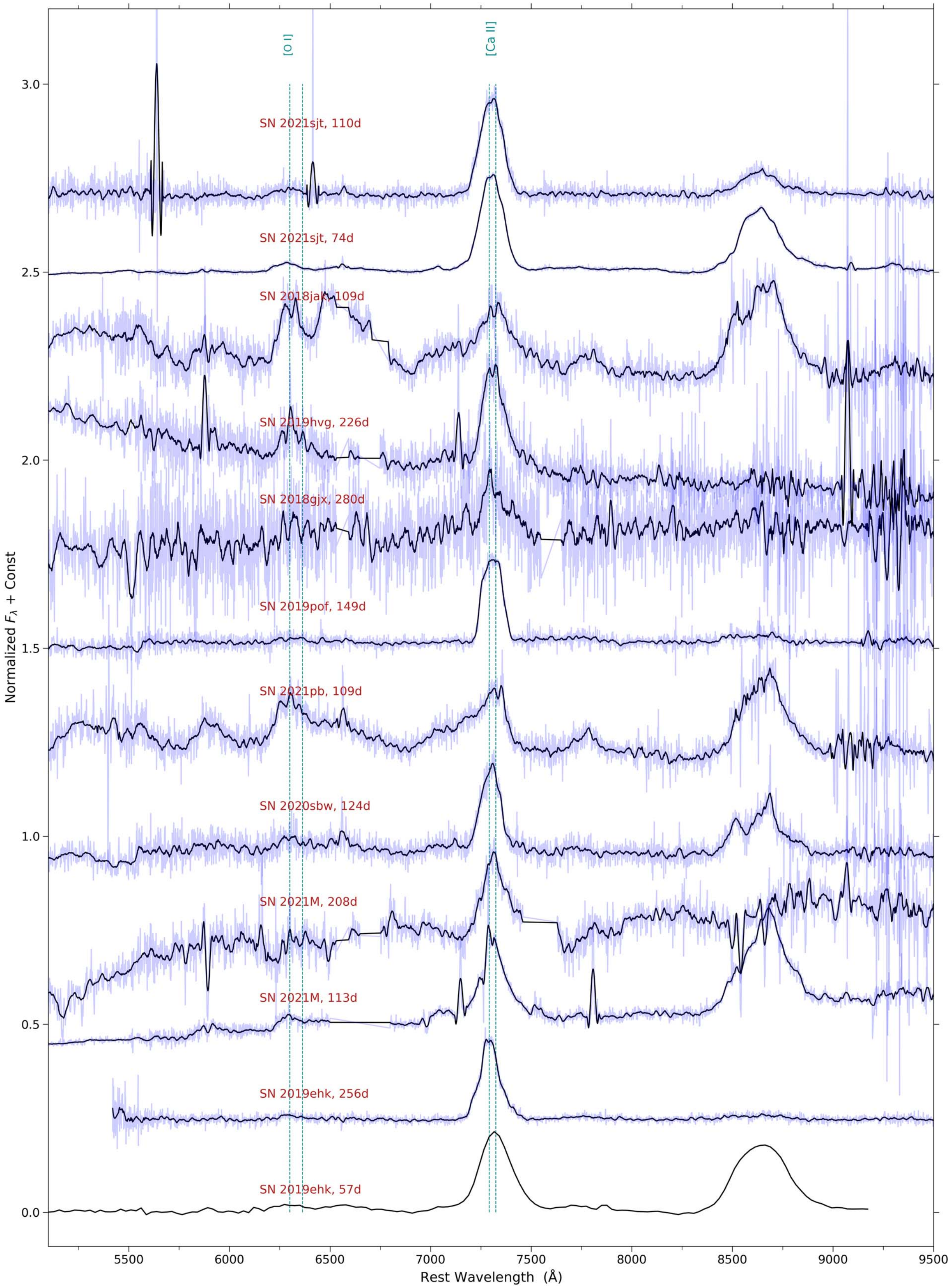

Figure 17. The full wavelength range of the nebular spectra shown in Figure 3. The phase of the spectra is measured as the number of rest-frame days since the second peak.

Appendix C
Light-curve Modeling Fits

Figure 18 shows a collage of the best-fit light curves for the shock-cooling model (Piro et al. 2021) fits to the multiband photometry data. Figure 19 shows a collage of the best-fit light curves for the radioactive peak model (Arnett et al. 1989) fits to the bolometric luminosity data.

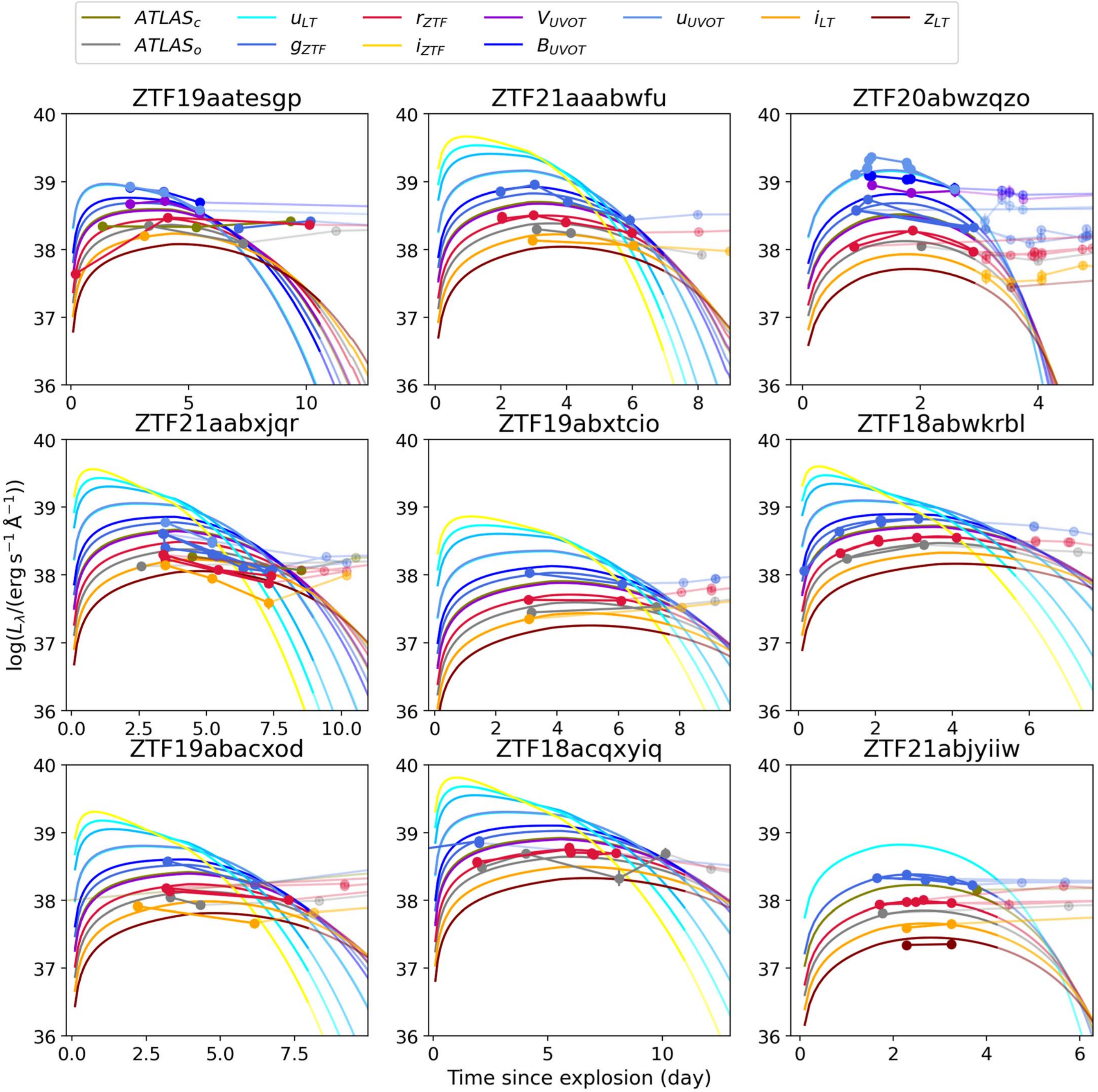

Figure 18. Shock-cooling model (Piro et al. 2021) fits to multiband data.

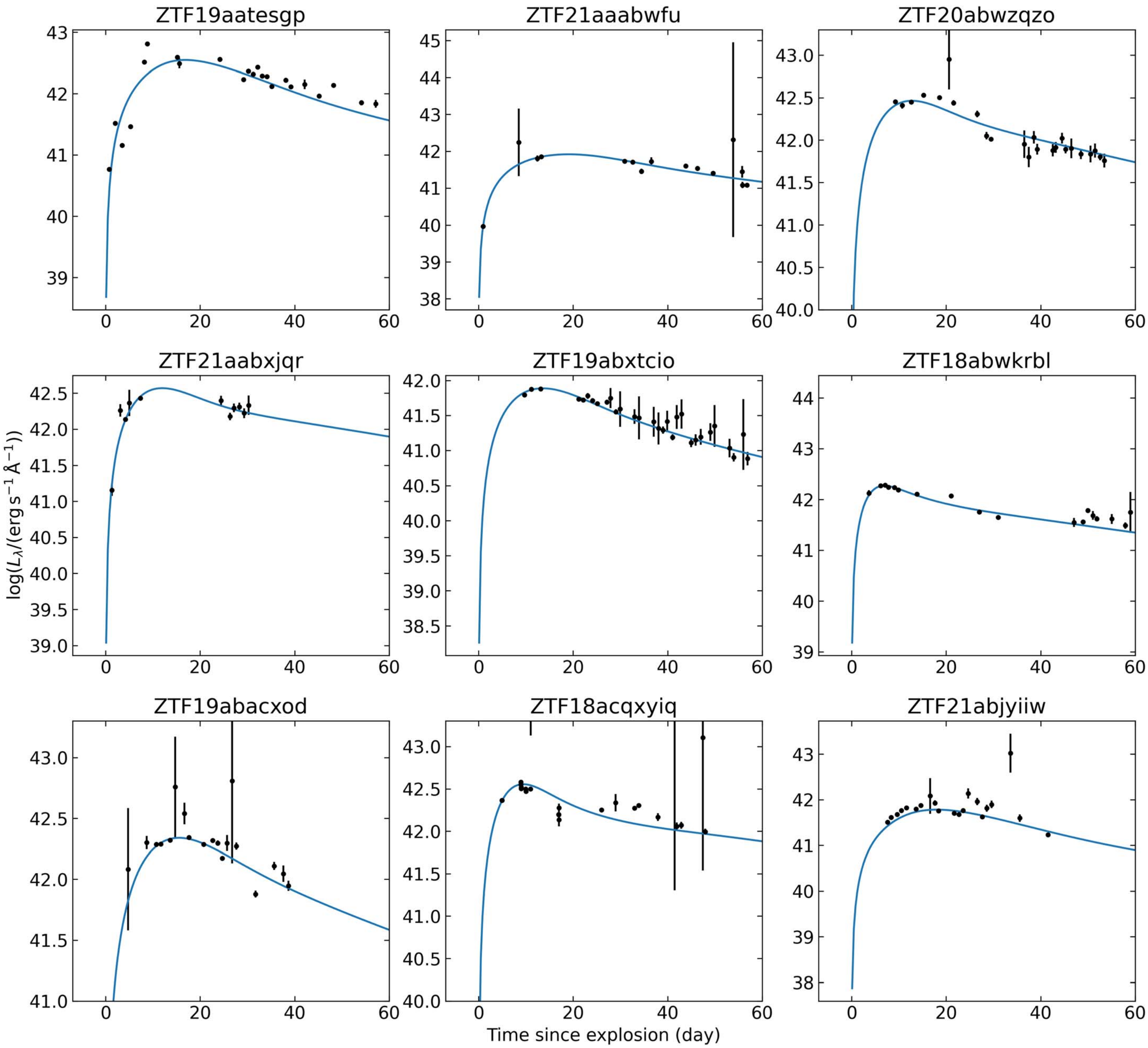

Figure 19. Radioactive (Arnett et al. 1989) fits to bolometric luminosity data excluding the data points fit by shock cooling.

Appendix D
Blackbody Fits

All the best-fit parameters, including bolometric luminosity, radius, and temperature for each object, are provided as machine-readable tables here. A truncated version of the summary of the blackbody properties for SN 2021sjt is shown in Table 7.

Table 7
Summary of the Photometry Data Used for SN 2021sjt (Truncated)

Source	Date (JD)	Filter (AB mag)	Mag. (AB mag)	Limiting Mag. (AB mag)
ZTF21abjyiiw	2459397.43	ztfg	*nan*	20.28
ZTF21abjyiiw	2459400.39	ztfg	*nan*	20.58
ZTF21abjyiiw	2459400.43	ztfr	*nan*	20.18
ZTF21abjyiiw	2459402.35	ztfg	18.58 ± 0.08	19.74
ZTF21abjyiiw	2459402.35	ztfg	18.58 ± 0.08	19.74
ZTF21abjyiiw	2459402.40	ztfr	18.01 ± 0.06	19.36

Note. The photometry and spectroscopy data for each object will be provided as machine-readable tables after publication here.

(This table is available in its entirety in machine-readable form.)

Appendix E
Photometry and Spectroscopy Data

All the photometry and spectroscopy data are provided as machine-readable tables here. A truncated version of the photometry table for SN 2021sjt is shown in Table 8.

Table 8
Summary of the Blackbody Properties for SN 2021sjt (Truncated)

Phase (days since first detection)	Log Luminosity (erg s^{-1})	Temperature (K)	Radius ($R_\odot$)
2	$42.34^{+0.56}_{-0.21}$	14615^{+12882}_{-4534}	3728^{+2424}_{-1711}
3	$42.10^{+0.02}_{-0.02}$	8449^{+520}_{-438}	8445^{+786}_{-774}
5	$42.08^{+0.01}_{-0.01}$	7118^{+340}_{-321}	11716^{+1013}_{-912}
6	$42.07^{+0.01}_{-0.01}$	6580^{+252}_{-242}	13412^{+1001}_{-912}

Note. All the best-fit parameters, including bolometric luminosity, radius, and temperature for each object, will be provided as machine-readable tables after publication here.

(This table is available in its entirety in machine-readable form.)

Appendix F
Host Galaxy Modeling

The models used for CIGALE and the summary of the host galaxy best-fit parameters are provided in Tables 9 and 10, respectively.

Table 9
The Models and Fitting Parameters Used for CIGALE

Galaxy Attributes	Brief Description
SFH	SFR $\propto \frac{t}{\tau^2}\exp(-t/\tau)$ $\tau = 250, 500, 1000, 2000, 4000, 6000, 8000$ Myr Age $t = 250, 500, 1000, 2000, 4000, 8000, 12,000$ Myr
SSP models	BC03 (Bruzual & Charlot 2003) + Chabrier IMF (Chabrier 2003) Stellar metallicity=0.0004, 0.004, 0.008, 0.02 $Z_\odot$
Dust attenuation	Modified power-law curves (Calzetti et al. 2000) + differential reddening of stars according to age $E(B-V)_{\rm young} = 0.0, 0.2, 0.3, 0.5, 0.8, 1.0, 1.5, 2.0, 3.0$ $E(B-V)_{\rm old} = 0.3, 0.50, 1.0$ UV − bump wavelength = 217.5 nm UV − bump amplitude = 0.0, 1.0, 2.0, 3.0 power-law slope = −0.13, −0.2, −0.5
Dust emission	Dust templates of Dale et al. (2014) + energy balance AGN fraction = 0 alpha = 1.0, 1.5, 2.0, 2.5
Nebular	$\log U_{\rm ion} = -2.0$ emission line width = 300.0 km s^{-1}

Table 10
Summary of the Host Galaxy Best-fit Parameters

ZTF Name	log Mass ($M_\odot$)	log SFR ($M_\odot$ yr^{-1})	*B*-band Abs. Mag. (mag)
SN 2019ehk/ZTF19aatesgp	$11.09^{+0.01}_{-0.00}$	$0.23^{+0.01}_{-0.00}$	−21.87
SN 2021M/ZTF21aaabwfu	$9.88^{+0.11}_{-0.15}$	$0.21^{+0.29}_{-0.12}$	−18.75
SN 2020sbw/ ZTF20abwzqzo	$10.71^{+0.06}_{-0.01}$	$-0.17^{+0.07}_{-0.01}$	−20.14
SN 2021pb/ZTF21aabxjqr	$10.74^{+0.20}_{-0.04}$	$0.67^{+0.16}_{-0.29}$	−21.17
SN 2019pof/ZTF19abxtcio	$8.62^{+0.01}_{-0.01}$	$-2.32^{+0.09}_{-0.07}$	−15.67
SN 2018gjx/ZTF18abwkrbl	$10.25^{+0.11}_{-0.11}$	$0.42^{+0.21}_{-0.12}$	−19.84
SN 2019hvg/ZTF19abacxod	$9.93^{+0.11}_{-0.13}$	$0.55^{+0.09}_{-0.17}$	−20.15
SN 2018jak/ZTF18acqxyiq	$9.84^{+0.26}_{-0.36}$	$1.09^{+0.55}_{-0.23}$	−19.52
SN 2021sjt/ZTF21abjyiiw	$10.70^{+0.18}_{-0.39}$	$2.11^{+1.44}_{-0.99}$	−16.78

ORCID iDs

Kaustav K. Das https://orcid.org/0000-0001-8372-997X
Mansi M. Kasliwal https://orcid.org/0000-0002-5619-4938
Christoffer Fremling https://orcid.org/0000-0002-4223-103X
Sheng Yang https://orcid.org/0000-0003-1546-6615
Steve Schulze https://orcid.org/0000-0001-6797-1889
Jesper Sollerman https://orcid.org/0000-0003-1546-6615
Tawny Sit https://orcid.org/0000-0001-8208-9755
Kishalay De https://orcid.org/0000-0002-8989-0542
Anastasios Tzanidakis https://orcid.org/0000-0003-0484-3331
Daniel A. Perley https://orcid.org/0000-0001-8472-1996
Shreya Anand https://orcid.org/0000-0003-3768-7515
Igor Andreoni https://orcid.org/0000-0002-8977-1498
C. Barbarino https://orcid.org/0000-0002-3821-6144
Andrew Drake https://orcid.org/0000-0003-0228-6594
Avishay Gal-Yam https://orcid.org/0000-0002-3653-5598
Russ R. Laher https://orcid.org/0000-0003-2451-5482
Viraj Karambelkar https://orcid.org/0000-0003-2758-159X
S. R. Kulkarni https://orcid.org/0000-0001-5390-8563
Frank J. Masci https://orcid.org/0000-0002-8532-9395
Michael S. Medford https://orcid.org/0000-0002-7226-0659
Abigail Polin https://orcid.org/0000-0002-1633-6495
Reed Riddle https://orcid.org/0000-0002-0387-370X
Yashvi Sharma https://orcid.org/0000-0003-4531-1745
Roger Smith https://orcid.org/0000-0001-7062-9726
Lin Yan https://orcid.org/0000-0003-1710-9339
Yi Yang https://orcid.org/0000-0002-6535-8500
Yuhan Yao https://orcid.org/0000-0001-6747-8509

References

Ahn, C. P., Alexandroff, R., Allende Prieto, C., et al. 2012, ApJS, 203, 21
Arnett, W. D., Bahcall, J. N., Kirshner, R. P., & Woosley, S. E. 1989, ARA&A, 27, 629
Barnsley, R. M., Smith, R. J., & Steele, I. A. 2012, AN, 333, 101
Bellm, E. C., Kulkarni, S. R., Graham, M. J., et al. 2019, PASP, 131, 018002
Bellm, E. C., & Sesar, B., 2016 pyraf-dbsp: Reduction pipeline for the Palomar Double Beam Spectrograph, Astrophysics Source Code Library, ascl:1602.002
Blagorodnova, N., Neill, J. D., Walters, R., et al. 2018, PASP, 130, 035003
Blanton, M. R., & Roweis, S. 2007, AJ, 133, 734
Blondin, S., & Tonry, J. L. 2007, in AIP Conf. Proc. 924, The Multicolored Landscape of Compact Objects and Their Explosive Origins, ed. T. di Salvo et al. (Melville, NY: AIP), 312
Boquien, M., Burgarella, D., Roehlly, Y., et al. 2019, A&A, 622, A103
Brown, T. M., Baliber, N., Bianco, F. B., et al. 2013, PASP, 125, 1031
Bruzual, G., & Charlot, S. 2003, MNRAS, 344, 1000
Burgarella, D., Buat, V., & Iglesias-Páramo, J. 2005, MNRAS, 360, 1413
Burrows, A., Radice, D., & Vartanyan, D. 2019, MNRAS, 485, 3153
Burrows, A., Radice, D., Vartanyan, D., et al. 2020, MNRAS, 491, 2715
Burrows, A., & Vartanyan, D. 2021, Natur, 589, 29
Calzetti, D., Armus, L., Bohlin, R. C., et al. 2000, ApJ, 533, 682
Cardelli, J. A., Clayton, G. C., & Mathis, J. S. 1989, ApJ, 345, 245
Cenko, S. B., Fox, D. B., Moon, D.-S., et al. 2006, PASP, 118, 1396
Chabrier, G. 2003, PASP, 115, 763
Chambers, K. C., Magnier, E. A., Metcalfe, N., et al. 2016, arXiv:1612.05560
Cook, D. O., Kasliwal, M. M., Van Sistine, A., et al. 2019, ApJ, 880, 7
Cutri, R. M., Wright, E. L., Conrow, T., et al. 2013, Explanatory Supplement to the AllWISE Data Release Products
Dale, D. A., Helou, G., Magdis, G. E., et al. 2014, ApJ, 784, 83
De, K., Fremling, U. C., Gal-Yam, A., et al. 2021, ApJL, 907, L18
De, K., Kasliwal, M. M., Cantwell, T., et al. 2018, ApJ, 866, 72
De, K., Kasliwal, M. M., Tzanidakis, A., et al. 2020, ApJ, 905, 58
Dekany, R., Smith, R. M., Riddle, R., et al. 2020, PASP, 132, 038001
Dessart, L., & Hillier, D. J. 2020, A&A, 642, A33
Dessart, L., Hillier, D. J., Sukhbold, T., Woosley, S. E., & Janka, H. T. 2021, A&A, 656, A61
Dewi, J. D. M., & Pols, O. R. 2003, MNRAS, 344, 629
Dewi, J. D. M., Pols, O. R., Savonije, G. J., & van den Heuvel, E. P. J. 2002, MNRAS, 331, 1027
Djupvik, A. A., & Andersen, J. 2010, Highlights of Spanish Astrophysics V, Vol. 14 (Berlin: Springer), 211
Elbaz, D., Daddi, E., Le Borgne, D., et al. 2007, A&A, 468, 33
Elmhamdi, A. 2011, AcA, 61, 179
Ergon, M., & Fransson, C. 2022, A&A, 666, A104
Ertl, T., Woosley, S. E., Sukhbold, T., & Janka, H. T. 2020, ApJ, 890, 51
Faber, S. M., Willmer, C. N. A., Wolf, C., et al. 2007, ApJ, 665, 265
Fang, Q., Maeda, K., Kuncarayakti, H., et al. 2022, ApJ, 928, 151
Fang, Q., Maeda, K., Kuncarayakti, H., Sun, F., & Gal-Yam, A. 2019, NatAs, 3, 434
Foreman-Mackey, D., Hogg, D. W., Lang, D., & Goodman, J. 2013, PASP, 125, 306
Fransson, C., & Chevalier, R. A. 1989, ApJ, 343, 323
Fremling, C., Miller, A. A., Sharma, Y., et al. 2020, ApJ, 895, 32
Fremling, C., Sollerman, J., Kasliwal, M. M., et al. 2018, A&A, 618, A37
Fremling, C., Sollerman, J., Taddia, F., et al. 2016, A&A, 593, A68
Gehrels, N., Chincarini, G., Giommi, P., et al. 2004, ApJ, 611, 1005
Graham, M. J., Kulkarni, S. R., Bellm, E. C., et al. 2019, PASP, 131, 078001
Grzegorzek, J. 2018, Transient Name Server Discovery Report, 2018-2018
Hachinger, S., Mazzali, P. A., Taubenberger, S., et al. 2012, MNRAS, 422, 70
Howell, D. A., Sullivan, M., Perrett, K., et al. 2005, ApJ, 634, 1190
Ilbert, O., Tresse, L., Zucca, E., et al. 2005, A&A, 439, 863
Jacobson-Galán, W. V., Margutti, R., Kilpatrick, C. D., et al. 2020, ApJ, 898, 166
Jacobson-Galán, W. V., Margutti, R., Kilpatrick, C. D., et al. 2021, ApJL, 908, L32
Janka, H.-T. 2012, ARNPS, 62, 407
Jerkstrand, A., Ergon, M., Smartt, S. J., et al. 2015, A&A, 573, A12
Jerkstrand, A., Smartt, S. J., Fraser, M., et al. 2014, MNRAS, 439, 3694
Kasliwal, M. M., Kulkarni, S. R., Gal-Yam, A., et al. 2012, ApJ, 755, 161
Kawabata, K. S., Maeda, K., Nomoto, K., et al. 2010, Natur, 465, 326
Khatami, D. K., & Kasen, D. N. 2019, ApJ, 878, 56
Kozyreva, A., Janka, H.-T., Kresse, D., Taubenberger, S., & Baklanov, P. 2022, MNRAS, 514, 4173
Lang, D. 2014, AJ, 147, 108
Laplace, E., Götberg, Y., de Mink, S. E., Justham, S., & Farmer, R. 2020, A&A, 637, A6
Limongi, M., & Chieffi, A. 2003, ApJ, 592, 404
Lunnan, R., Kasliwal, M. M., Cao, Y., et al. 2017, ApJ, 836, 60
Maeda, K., Kawabata, K., Tanaka, M., et al. 2007, ApJL, 658, L5
Mainzer, A., Bauer, J., Cutri, R. M., et al. 2014, ApJ, 792, 30
Martin, D. C., Fanson, J., Schiminovich, D., et al. 2005, ApJL, 619, L1
Masci, F. J., Laher, R. R., Rusholme, B., et al. 2019, PASP, 131, 018003
Meisner, A. M., Lang, D., & Schlegel, D. J. 2017, AJ, 153, 38
Melson, T., Janka, H.-T., & Marek, A. 2015, ApJL, 801, L24
Milisavljevic, D., Patnaude, D. J., Raymond, J. C., et al. 2017, ApJ, 846, 50
Moriya, T., Tominaga, N., Tanaka, M., et al. 2010, ApJ, 719, 1445
Moriya, T. J., Mazzali, P. A., Tominaga, N., et al. 2017, MNRAS, 466, 2085
Nakaoka, T., Maeda, K., Yamanaka, M., et al. 2021, ApJ, 912, 30
Nakar, E., & Piro, A. L. 2014, ApJ, 788, 193
Noll, S., Burgarella, D., Giovannoli, E., et al. 2009, A&A, 507, 1793
Nomoto, K. 1984, ApJ, 277, 791
Nomoto, K., Hashimoto, M., Tsujimoto, T., et al. 1997, NuPhA, 616, 79
Nomoto, K., Sparks, W. M., Fesen, R. A., et al. 1982, Natur, 299, 803
Oke, J. B., & Gunn, J. E. 1982, PASP, 94, 586
O'Neill, D., Kotak, R., Fraser, M., et al. 2021, A&A, 645, L7
Perets, H. B., Gal-yam, A., Crockett, R. M., et al. 2011, ApJL, 728, L36
Perley, D. A. 2019, PASP, 131, 084503
Perley, D. A., Fremling, C., Sollerman, J., et al. 2020, ApJ, 904, 35
Phillips, M. M., Simon, J. D., Morrell, N., et al. 2013, ApJ, 779, 38
Piascik, A. S., Steele, I. A., Bates, S. D., et al. 2014, Proc. SPIE, 9147, 91478H
Piro, A. L. 2015, ApJL, 808, L51
Piro, A. L., Haynie, A., & Yao, Y. 2021, ApJ, 909, 209
Podsiadlowski, P., Han, Z., & Rappaport, S. 2003, MNRAS, 340, 1214
Podsiadlowski, P., Langer, N., Poelarends, A. J. T., et al. 2004, ApJ, 612, 1044
Polin, A., Nugent, P., & Kasen, D. 2021, ApJ, 906, 65
Poznanski, D., Ganeshalingam, M., Silverman, J. M., & Filippenko, A. V. 2011, MNRAS, 415, L81
Poznanski, D., Prochaska, J. X., & Bloom, J. S. 2012, MNRAS, 426, 1465
Prentice, S. J., Maguire, K., Siebenaler, L., & Jerkstrand, A. 2022, MNRAS, 514, 5686

Prochaska, J., Hennawi, J., Westfall, K., et al. 2020, JOSS, 5, 2308
Pumo, M. L., Turatto, M., Botticella, M. T., et al. 2009, ApJL, 705, L138
Rabinak, I., & Waxman, E. 2011, ApJ, 728, 63
Rauscher, T., Heger, A., Hoffman, R. D., & Woosley, S. E. 2002, ApJ, 576, 323
Reguitti, A., Pumo, M. L., Mazzali, P. A., et al. 2021, MNRAS, 501, 1059
Rigault, M., Neill, J. D., Blagorodnova, N., et al. 2019, A&A, 627, A115
Roberson, M., Fremling, C., & Kasliwal, M. 2022, JOSS, 7, 3612
Roming, P. W. A., Kennedy, T. E., Mason, K. O., et al. 2005, SSRv, 120, 95
Schlafly, E. F., & Finkbeiner, D. P. 2011, ApJ, 737, 103
Schulze, S., Yaron, O., Sollerman, J., et al. 2021, ApJS, 255, 29
Siebert, M. R., Davis, K., Tinyanont, S., Foley, R. J., & Strasburger, E. 2021, Transient Name Server Classification Report, 2021-2383
Skrutskie, M. F., Cutri, R. M., Stiening, R., et al. 2006, AJ, 131, 1163
Smartt, S. J., Eldridge, J. J., Crockett, R. M., & Maund, J. R. 2009, MNRAS, 395, 1409
Smartt, S. J., Valenti, S., Fraser, M., et al. 2015, A&A, 579, A40
Smith, K. W., Smartt, S. J., Young, D. R., et al. 2020, PASP, 132, 085002
Sollerman, J., Leibundgut, B., & Spyromilio, J. 1998, A&A, 337, 207
Sravan, N., Marchant, P., & Kalogera, V. 2019, ApJ, 885, 130
Steele, I. A., Smith, R. J., Rees, P. C., et al. 2004, Proc. SPIE, 5489, 679
Stockinger, G., Janka, H. T., Kresse, D., et al. 2020, MNRAS, 496, 2039
Stritzinger, M. D., Taddia, F., Burns, C. R., et al. 2018, A&A, 609, A135
Sukhbold, T., Ertl, T., Woosley, S. E., Brown, J. M., & Janka, H. T. 2016, ApJ, 821, 38
Taddia, F., Stritzinger, M. D., Bersten, M., et al. 2018, A&A, 609, A136
Taggart, K., & Perley, D. A. 2021, MNRAS, 503, 3931
Tauris, T. M., Langer, N., Moriya, T. J., et al. 2013, ApJL, 778, L23
Tauris, T. M., Langer, N., & Podsiadlowski, P. 2015, MNRAS, 451, 2123
Tonry, J. L., Denneau, L., Heinze, A. N., et al. 2018, PASP, 130, 064505
Toonen, S., Perets, H. B., Igoshev, A. P., Michaely, E., & Zenati, Y. 2018, A&A, 619, A53
Uomoto, A. 1986, ApJL, 310, L35
Valenti, S., Benetti, S., Cappellaro, E., et al. 2008, MNRAS, 383, 1485
Valerin, G., Pumo, M. L., Pastorello, A., et al. 2022, MNRAS, 513, 4983
Van Dyk, S. D. 2017, in Handbook of Supernovae, ed. A. W. Alsabti & P. Murdin (Berlin: Springer), 693
Wheeler, J. C., Johnson, V., & Clocchiatti, A. 2015, MNRAS, 450, 1295
Woosley, S. E. 2019, ApJ, 878, 49
Woosley, S. E., & Heger, A. 2015, ApJ, 810, 34
Wright, A. H., Robotham, A. S. G., Bourne, N., et al. 2016, MNRAS, 460, 765
Wright, E. L., Eisenhardt, P. R. M., Mainzer, A. K., et al. 2010, AJ, 140, 1868
Yang, S., Sollerman, J., Strotjohann, N. L., et al. 2021, A&A, 655, A90
Yao, Y., De, K., Kasliwal, M. M., et al. 2020, ApJ, 900, 46
Yaron, O., & Gal-Yam, A. 2012, PASP, 124, 668
Yoon, S.-C., Woosley, S. E., & Langer, N. 2010, ApJ, 725, 940
Yoshida, T., Suwa, Y., Umeda, H., Shibata, M., & Takahashi, K. 2017, MNRAS, 471, 4275
Zapartas, E., de Mink, S. E., Izzard, R. G., et al. 2017, A&A, 601, A29
Zenati, Y., Toonen, S., & Perets, H. B. 2019, MNRAS, 482, 1135